Robust Optimization of RIS in Terahertz under Extreme Molecular Re-radiation Manifestations

Anish Pradhan, Mohamed A. Abd-Elmagid, Harpreet S. Dhillon and Andreas F. Molisch

***Abstract*—Terahertz (THz) communication signals are susceptible to severe degradation because of the molecular interaction with the atmosphere in the form of subsequent absorption and re-radiation. Recently, reconfigurable intelligent surface (RIS) has emerged as a potential technology to assist in THz communications by boosting signal power or providing virtual line-of-sight (LOS) paths. However, the re-radiated energy has either been modeled as a scattering component or as additive Gaussian noise in the literature. Since the precise characterization is still a work in progress, this paper presents the first comparative investigation of the performance of an RIS-aided THz system under these two extreme re-radiation models. In particular, we first develop a novel parametric channel model that encompasses both models of the re-radiation through a simple parameter change, and then utilize that to design a robust block-coordinate descent (BCD) algorithmic framework which maximizes a lower bound on channel capacity while accounting for imperfect channel state information (CSI). In this framework, the original problem is split into two sub-problems: a) receive beamformer optimization, and b) RIS phase-shift optimization. As the latter sub-problem (unlike the former) has no analytical solution, we propose three approaches for it: a) semi-definite relaxation (SDR) (high complexity), b) signal alignment (SA) (low complexity), and c) gradient descent (GD) (low complexity). The time complexities associated with the proposed approaches are explicitly derived. We analytically demonstrate the limited interference suppression capability of a passive RIS by deriving the stationary points of signal-to-interference and noise ratio (SINR) of a one-element RIS system with one interferer. Our numerical results also demonstrate that slightly better throughput is achieved when the re-radiation manifests as scattering.**

***Index Terms*—Reconfigurable intelligent surface, terahertz, molecular re-radiation, imperfect CSI, robust optimization.**

I. Introduction

With the standardization of 5G new radio (NR), it is now well-accepted that the traditional sub-6 GHz spectrum by itself is not sufficient to meet the ever-expanding network demands in the near future [2], [3]. This has led to the pursuit of utilizing higher frequency bands, which ultimately resulted in the recent commercialization of mmWave communication. However, with the advent of extended reality (xR) technologies, even higher data rates - up to 1 Tbit/s - for which mmWave bandwidths are not sufficient anymore, are required [4]. The reason is that the xR ecosystem imposes very stringent requirements on the throughput of the wireless communication technologies sustaining it. Once realized, the xR applications are expected to revolutionize many industry sectors, including, but not limited to, healthcare, entertainment, and eCommerce. To support such applications, there has been a recent interest in exploring the possibility of utilizing the THz (0.1-10 THz) spectrum, which lies above the mmWave band [2]. Recent breakthroughs in the research of high-power THz sources [5], [6] have further increased the viability of utilizing this spectrum.

However, THz communication links are highly susceptible to blockages, both by static objects and by dynamic objects including the users operating the VR [7]. Static blockages consistently prevent the suitable quality of experience (QoE), while dynamic blockages result in a sudden decrease in throughput and are detrimental to the immersion of xR. Moreover, molecular re-radiation can impact THz signals by manifesting as either noise or scattering components.

Inspired by the recent standardization efforts by various organizations, a potential solution is to deploy the emerging RIS technology that can create virtual LOS links to enhance throughput in situations where direct LOS links are blocked. Yet, the integration of RIS with THz communication links presents the following challenges: a) accurate characterization of the molecular re-radiation, b) channel estimation issues due to RIS, and c) subsequent operation of RIS under imperfect CSI. To overcome these challenges, we first develop a parametric THz channel model in this paper that captures both manifestations of re-radiation, and then use that model to present a novel alternating RIS optimization framework, where the RIS phase-shift and receive beamformer are jointly optimized.

A. Background and Prior Art

We will now discuss in more detail each of the aforementioned challenges associated with integrating RIS with THz communication links. We start this discussion with the challenge of accurate characterization of the molecular re-radiation, which is less understood and is also the prime motivation behind this work. In most of our typical communication scenarios, water vapor is one of the primary constituents in the molecular makeup of the wireless medium. Since water molecule, like many other atmospheric molecules [8], has many rotational absorption lines through the THz band [9], these molecules are highly susceptible to being excited by the THz communication signals. In particular, the transmitted EM wave causes molecular absorption by exciting the molecules

A. Pradhan, M. A. Abd-Elmagid, and H. S. Dhillon are with Wireless@VT, Department of ECE, Virginia Tech, Blacksburg, VA, USA (email: {pradhananish1, maelaziz, hdhillon}@vt.edu). A. F. Molisch is with the Wireless Devices and Systems Group, Ming Hsieh Department of Electrical and Computer Engineering, University of Southern California, Los Angeles, CA, USA (email: molisch@usc.edu). This work was supported by U.S. National Science Foundation under Grant ECCS-2030215. This paper was presented in part at the IEEE Globecom 2021, Madrid, Spain [1].

from lower to higher energy states. These higher energy molecules re-radiate absorbed energy in a similar frequency range while returning to the ground state. For many decades, the process of such atomic and molecule re-radiation has been referred to as *radiation trapping* in the physics literature [10]. In the existing THz literature, this re-radiation often manifests as additive Gaussian noise based on *sky-noise* models [8], [11]. This is an approximation that results from the fundamental difference of the physical phenomena dictating the two [8]. To our knowledge, no measurement studies have adequately supported this model until now. Furthermore, there is some support in the literature [8], [12], [13] for describing this phenomenon as scattering, with the presence of multiple scattered copies of the signal due to re-radiation. Note that this scattering could potentially result in delay dispersion [8] and frequency dispersion [10], which is beyond the scope of this paper. Following the scattering assumption, [14] recently characterized the THz channel as a Rician channel, with the Rician factor computed from the molecule absorption coefficient. In the literature, both manifestations (i.e., as noise and as scattering) have been employed separately, and determining the prevalence of each effect is difficult. To be more specific, the exact effect will most likely exist as a combination of these two extreme situations and depends solely on the medium and its molecular constituents. There is no way to accurately define the exact effect without comprehensive measurement studies. It is worth mentioning that the scattering assumption, being at one of the extremes of the modeling spectrum, might represent an extreme that is not achievable in practice. Nevertheless, given the current information, one of the reasonable things to do with the current information is to explore the two extreme circumstances and quantify their influence on the RIS performance which is what we do in this paper.

Due to the peculiarities of the THz links, the techniques developed in the beamforming literature on RIS [15]–[21] in the sub-6 GHz spectrum (that deal with the joint optimization of RIS phase-shifts and receiver beamformer) cannot be trivially extended. The interplay between RIS and THz band has been recently studied in [7], [22]–[27]. The authors of [22] proposed a sub-optimal search method to optimize RIS discrete phase-shifts while the authors of [23] jointly optimized the RIS location, phase-shift and THz sub-bands to improve system performance. A deep reinforcement learning-based algorithm has been used to optimize the reliability and rate for RIS-operated virtual reality systems in the THz band [7]. A physically consistent near-field channel model for RIS-THz systems was developed in [24] while the secrecy rate for an RIS-aided THz system was optimized in [25]. A particle swarm optimization-based method with limited channel estimation was used to optimize the RIS phase-shifts in a THz band [26]. The error performance of an RIS-assisted low earth orbit satellite network has been analyzed in [27]. However, the above prior works studying RIS in the THz band neglected either the two possible manifestations of the molecular re-radiation, or the cumulative effect of this re-radiation along with the RIS configuration on the receiver noise [7], [22]–[27]. Further, they did not account for the natural challenge of imperfect CSI resulting from the passive nature of RIS elements, and non-cooperation from the interfering nodes. In light of these limitations, our work is particularly valuable for RIS-aided use cases where a precise understanding and modeling of molecular re-radiation is essential to ensure good performance.

The robust optimization of RIS-aided THz systems (against the imperfect CSI) has only been considered in a handful of recent works [28]–[30]. These works used semidefinite programming (SDP) techniques while ignoring the peculiar characteristics of RIS-THz integration. Such techniques suffer from high computational cost that decreases the energy efficiency of the network, and hence defeat the purpose of low-cost RISs [31]. We bridge this gap by developing a parametric THz channel model that accounts for both assumptions of re-radiation, as well as three BCD-based joint optimization approaches of varying complexity for the proposed channel model under imperfect CSI. We use a lower bound on the channel capacity as our objective as the exact channel capacity is unknown for considering interference in our system model [32]. Different from [28], [29], the achievable throughput expression in our objective function assumes that the receiver only has access to imperfect CSI, which reflects the reality more precisely. Our objective function is also consistent with the discussion of the uplink spectral efficiency under imperfect CSI in [32, Eq. (4.1)]. To the best of our knowledge, no comparative study exists that analyzes a jointly-optimized multi-antenna system in a THz environment with two extreme assumptions regarding molecule re-radiation.

B. Contributions

We study an RIS-aided THz system setting that consists of a single-stream transmitter (Tx) communicating with an RIS-aided multi-antenna receiver (Rx) in the THz band in the presence of potentially multiple single-stream interferers. For this setup, our objective is to jointly optimize the RIS's phase-shift and receive beamformer while assuming imperfect CSI knowledge. Our key contributions in this paper are listed next.

A novel parametric THz channel. We propose a new parametric THz channel model that accounts for the following two extreme manifestations of re-radiation in the THz spectrum through a single parameter change: a) re-radiation is assumed as Gaussian noise, and b) re-radiation is assumed as an scattering component of the signal. We also characterize the cumulative effect of molecular re-radiation and the RIS configuration utilizing this parameter.

Three robust BCD algorithms. We formulate an optimization problem in which we jointly optimize the RIS's phase-shift vector and receive beamformer vector with the objective of maximizing a lower bound on the channel capacity. Due to the coupling between the two sets of optimization variables (i.e., the RIS's phase-shift vector and receive beamformer vector) in its objective function, the formulated problem turns out to be non-convex, and hence its global optimal solution cannot be obtained using standard convex optimization techniques. Because of that, we aim to obtain an efficient solution through the BCD algorithm. In this algorithm, we split the original problem of two sets of optimization variables

into the following two sub-problems of one set of variables each: a) receive beamforming vector optimization problem, and b) RIS's phase-shift optimization problem. These sub-problems are then solved in an alternative manner until they converge to an efficient solution of the original problem. As the latter sub-problem does not have a closed-form solution unlike the former, we propose three algorithms of varying complexity to solve the RIS sub-problem. First, we propose a conventional SDR approach as a baseline. Due to the high time complexity of the SDR approach, we then present the SA approach for its speed, where the expected receive signal strength is maximized rather than the original objective function. This approach provides a good sub-optimal solution when the interference power in the network is low. However, in a network with a moderate amount of interference, we can achieve better performance without sacrificing any speed by utilizing the gradient descent algorithm, which is our third proposed approach. These approaches consider the direct links of both users and interferers under imperfect CSI. Our objective function also caters to the non-robust counterpart by simply assuming no error. Finally, the time complexities associated with these approaches are explicitly derived.

System design insights. We analytically characterize the performance loss associated with the SA solution by deriving the stationary points of a one-element RIS-aided system with one interferer. This allows us to demonstrate that the passive RIS has limited capability to suppress interference when the direct link of the interferer is much stronger than the reflected link. Multiple system design insights can also be drawn from the numerical results. For example, our numerical results reveal that when re-radiation manifests as scattering, the corresponding throughput of the optimized system is slightly higher than when it manifests as noise. They also show that the gap in performance of the two cases depends on the visibility of the interferer direct links and frequency. Under perfect CSI, throughput is shown to increase linearly and logarithmically with the increasing number of RIS elements and Rx antennas, respectively. Further, we do not observe much penalty in performance by assuming the nature of molecular re-radiation in the optimization method incorrectly whenever perfect CSI is available. The results also show that the proposed robust algorithms perform better than the non-robust counterparts under imperfect CSI. In particular, our results demonstrate that the BCD-GD algorithm is superior in terms of runtime and SER performance.

Notations: The scalar, vector and matrix are denoted by x, $\mathbf{x}$ and $\mathbf{X}$, respectively. All the vectors are column vectors unless stated explicitly. For a matrix $\mathbf{X}$, $\mathbf{X}^T$, $\mathbf{X}^H$, $\mathrm{Tr}\,(\mathbf{X})$, $[\mathbf{X}]_{i,j}$, $\mathrm{Re}\,(\mathbf{X})$ and $\mathbf{X} \succeq 0$ denote its transpose, conjugate transpose, trace, (i,j)-th element, real part and positive semidefiniteness, respectively. The operation $\mathrm{vec}(\mathbf{X})$ results in a vector with every element of $\mathbf{X}$. For a vector $\mathbf{x}$, $\mathrm{diag}\,(\mathbf{x})$ denotes the diagonal matrix with the elements of $\mathbf{x}$ as its diagonal elements. The element-wise product is denoted by $\odot$. The distribution of a standard complex normal random variable is denoted by $\mathcal{CN}(0,1)$.

II. System Model

We consider an RIS-aided THz system setup with multiple Tx-Rx pairs communicating simultaneously in the same THz frequency band, initially inspired by an indoor xR scenario, which can also be applied to describe RIS-aided device-to-device links. The Tx of interest (Tx_0) is assumed to be a single-stream device with constant transmitter gain $G_{Tx,0}$ and no active beamforming capabilities (possibly due to the small form factor or hardware limitations of VR/AR user equipment with multiple antennas) [33]. By the lack of active beamforming, we imply that the beamforming vector stays constant even when the channel conditions change; our assumption is that the beams are pointed at the RIS. After accounting for this gain, the effective channels are similar to single-antenna channels in mathematical formulation. The Rx of interest (Rx_0) is considered to have multiple antennas (similar to a mobile edge computing server) [7] and is assisted by a passive RIS. The multi-antenna Rx_0 has N_R receive antennas, while the RIS has N elements. Motivated by the literature and measurement results that indicate the existence of co-channel interference (CCI) in terahertz communications when different types of beamforming are used, we consider that there are N_I co-channel single-stream users with transmitter gain $G_{Tx,i}$ that interfere in the direction of Rx_0 [34], [35]. It is assumed that each of the communicating devices can have two paths to Rx_0, one link coming directly from the Tx, and another link reflected from the RIS. The system model is illustrated in Fig. 1. Note that the N_I interfering users are communicating with their own Rxs. These Rxs do not affect our analysis and are therefore not included in Fig. 1. Both RIS and Rx_0 are assumed to be uniform rectangular arrays (URAs) with half-wavelength spacing to sufficiently decrease mutual coupling [36]. The array response vector of a general URA with N_0 elements is defined as follows [32]:

$$\mathbf{a}_{N_0}(\varphi,\theta,\mathbf{U}_{node}) = \left[e^{j\mathbf{k}(\varphi,\theta)^T\mathbf{u}_1},\ldots,e^{j\mathbf{k}(\varphi,\theta)^T\mathbf{u}_{N_0}}\right], \quad (1)$$

where $\mathbf{k}(\varphi,\theta) = \frac{2\pi}{\lambda}\left[\cos(\theta)\cos(\varphi),\cos(\theta)\sin(\varphi),\sin(\theta)\right]^T$ is the wave vector, λ denotes the wavelength, $\mathbf{u}_i$ denotes the vector of Cartesian co-ordinates of the i-th URA element, and $\mathbf{U}_{node}$ denotes the matrix $[\mathbf{u}_1,\mathbf{u}_2,\ldots,\mathbf{u}_{N_0}]$. The azimuth angle $\varphi \in [-\pi,\pi)$ is measured from the positive x-axis and the elevation angle $\theta \in [-\frac{\pi}{2},\frac{\pi}{2})$ is measured from the x-y plane. The array is assumed to be on the positive y-z plane with the origin as the reference. Note that the array response vector is defined as a row vector.

A. Terahertz Channel Model

Owing to the molecular absorption phenomena in the THz band, a fraction $1-\tau(f,d)$ of the propagating signal is absorbed and re-radiated by the media. The remaining fraction $\tau(f,d) = e^{-k(f)d}$ is termed as the transmittance of the channel, where $k(f)$, f and d denote the molecular absorption coefficient, the operating frequency, and the link distance, respectively. Further, we use a simple LOS channel model that is valid for 200-450 GHz [37] for the molecular absorption coefficient calculation. We acknowledge that more involved

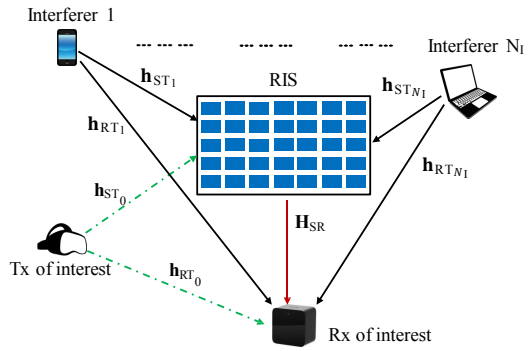

Fig. 1: System model for the RIS-assisted communication in THz.

channel models, such as those incorporating NLOS multipath components, could be considered in future work. However, given the added complexity and the relatively small accuracy boost that such models may provide, we believe that our current approach is both sufficient and insightful for the scope of our paper [38]. The equation dictating the value of $k(f)$ considering the simple LOS model is: $k(f) = \sum_i y_i(f,\mu) + g(f,\mu)$, where μ denotes the volume mixing ratio of water vapor, $y_i(f,\mu)$ denotes the absorption coefficient for the i-th absorption line, and the polynomial function $g(f,\mu)$ is an equalization factor. The volume mixing ratio μ can be calculated through the following equation:$\mu = \frac{\phi}{100}\frac{p_w(T,p)}{p}$, where ϕ and p denote the relative humidity and pressure, respectively. The function $p_w(T,p)$ can be described by the Buck equation [39]:

$$p_w(T,p) = 6.1121\left(1.0007 + 3.46\times10^{-6}p\right)\exp\left(\frac{17.502T}{240.97+T}\right), \tag{2}$$

where the pressure p is in hectopascals and the temperature T is in Celsius. Next, we express $\{y_i(f,\mu)\}$ and $g(f,\mu)$ as described in [37]:

$$y_1(f,\mu) = \frac{A(\mu)}{B(\mu)+\left(\frac{f}{100c}-p_1\right)}, y_2(f,\mu) = \frac{C(\mu)}{D(\mu)+\left(\frac{f}{100c}-p_2\right)},$$
$$y_3(f,\mu) = \frac{E(\mu)}{F(\mu)+\left(\frac{f}{100c}-p_3\right)}, y_4(f,\mu) = \frac{G(\mu)}{H(\mu)+\left(\frac{f}{100c}-p_4\right)},$$
$$g(f,\mu) = \frac{\mu}{0.0157}\left(q_1 f^4 + q_2 f^3 + q_3 f^2 + q_4 f + q_5\right),$$

where the frequency f is in Hertz and the various inner entities are described below:

$$\begin{aligned}
A(\mu) &= 0.2251\mu(0.1314\mu + 0.0297),\\
B(\mu) &= (0.4127\mu + 0.0932)^2,\\
C(\mu) &= 2.053\mu(0.1717\mu + 0.0306),\\
D(\mu) &= (0.5394\mu + 0.0961)^2,\\
E(\mu) &= 0.177\mu(0.0832\mu + 0.0213),\\
F(\mu) &= (0.2615\mu + 0.0668)^2,\\
G(\mu) &= 2.146\mu(0.1206\mu + 0.0277),\\
H(\mu) &= (0.3789\mu + 0.0871)^2.
\end{aligned}$$

The constants used are: $p_1 = 10.84\ \text{cm}^{-1}, p_2 = 12.68\ \text{cm}^{-1}, p_3 = 14.65\ \text{cm}^{-1}, p_4 = 14.94\ \text{cm}^{-1}$, $q_1 = 8.495\times10^{-48}, q_2 = -9.932\times10^{-36}, q_3 = 4.336\times10^{-24}, q_4 = -8.33\times10^{-13}$, and $q_5 = 5.953\times10^{-2}$. The absorption lines $y_1(f,\mu), y_2(f,\mu), y_3(f,\mu)$, and $y_4(f,\mu)$ represent the absorption peaks at center frequencies 325 GHz, 380 GHz, 439 GHz, and 448 GHz, respectively.

Recall from Section I that the absorbed power is emitted again in the same band, and there are two extreme modeling assumptions regarding how this molecular re-radiation manifests. Unlike the forward scattering we witness in visible light owing to tiny particles, this re-radiation occurs virtually isotropically, and the energy is spread in all directions for the THz band [40]. However, it is commonly assumed that the whole absorbed power is available at the Rx node through re-radiation [11], [14]. This result follows from the assumptions that a single absorption/re-radiation event occurs throughout the entire propagation route, and that all re-radiated power is directed in the direction of the Rx node, despite the fact that this is never explicitly stated. In our paper, we also apply these assumptions. The assumptions of the two extremes of molecular re-radiation are provided next for a more systematic exposition.

Assumption 1. *Molecular re-radiation is modeled as additive Gaussian noise.*

Assumption 2. *Molecular re-radiation is modeled as a scattering event where the affected channel response includes a scattering component.*

Remark 1. *When we design the system assuming a particular manifestation but that does not hold in reality, it will result in a channel mismatch and potential degradation in performance.*

The re-radiated signal, which has $1-\tau(f,d)$ of the total signal power appears as either additive noise or as the scattering component. Because of the nature of their modeling, the two assumptions are at opposite extremes of the spectrum, with reality falling somewhere in the middle. The Rician-like factor K_d in Assumption 2 for distance d is

$$K_d = \frac{\text{Power of the LOS component}}{\text{Power of the scattering component}} = \frac{G_{Tx,i}\tau(f,d)}{1-\tau(f,d)}, \tag{3}$$

where the diffused re-radiated component is isotropic in nature and does not include the transmitter gain. The two assumptions can also be interpreted as resulting from different possible receiver structures. Firstly, we have to recognize that radiation trapping generally leads to both delay and frequency dispersion, with the former arising from the finite lifetime of the excited molecular states, and the latter arising from (partial or complete) frequency redistribution occurring about relaxation of the excited state into the ground state [10]. If the frequency redistribution is over a band that is larger than the transmission bandwidth, part of the absorbed energy will be completely lost, while the remainder stays in the considered band. Depending on the amount of dispersion and its time variance, as well as the considered modulation and coding scheme, the scattered energy can be exploited for signal

detection, or act as interference. For this reason, this paper considers the two limiting cases of "fully useful" and "fully noise".

In contrast to the microwave spectrum, multipath propagation from environmental scatterers in the THz band experiences high reflection and scattering loss because diffraction occurs less often and the roughness of most surfaces is comparable to the wavelength. Due to these phenomena, wireless links in THz are often modeled as LOS channels in the literature which corresponds to Assumption 1 [29], [38], [41]. However, as demonstrated in [14], one can include the re-radiated component resulting from Assumption 2 to the existing LOS model in a Rician manner for a complete description of the channel when the re-radiation is treated as scattering. Although the mentioned re-radiated component is fundamentally different from the multipath-based NLOS component in a standard Rician formulation, the mathematical exposition of it in a channel model is similar to a standard Rician channel model. By including a variable ζ in the standard Rician channel model [14], we unify both Assumptions 1 and 2 concerning the re-radiation process for analytical convenience. In the first scenario, the unified model should only include the LOS component since the re-radiation signal appears as Gaussian noise, whereas the channel model in the second case should include both the LOS and scattering components because re-radiation appears as scattering. In other words, the models corresponding to Assumptions 1 and 2 can be recovered from the unified model by setting $\zeta = 1$ and $\zeta = 0$, respectively. Additionally, the phases of the re-radiated wave scattering components are influenced by molecular vibration, resulting in received power being affected by numerous phase-independent re-radiated photons. Consequently, the phases are assumed to be uniformly distributed in the $[0, 2\pi)$ range, leading to the i.i.d assumption [10], [14]. Further details on the modified Rician channel with the ζ parameter are provided next.

The channel response between X and Y is denoted by $\mathbf{h}_{\mathrm{XY}}$ or $\mathbf{H}_{\mathrm{XY}}$ (depending on the number of antenna elements at X and Y), and can be expressed as:

$$\mathbf{h}_{\mathrm{XY}} = \left(\sqrt{\frac{K_d}{K_d+1}}\mathbf{f}_{\mathrm{LOS}}e^{j\varpi} + \sqrt{\frac{1-\zeta}{K_d+1}}\tilde{\mathbf{h}}_{\mathrm{XY}}\right)\frac{c}{4\pi f d}, \quad (4)$$

$$\mathbf{H}_{\mathrm{XY}} = \left(\sqrt{\frac{K_d}{K_d+1}}\mathbf{F}_{\mathrm{LOS}}e^{j\varpi} + \sqrt{\frac{1-\zeta}{K_d+1}}\tilde{\mathbf{H}}_{\mathrm{XY}}\right)\frac{c}{4\pi f d}, \quad (5)$$

where ϖ denotes a random phase uniformly distributed in $[-\pi, \pi)$, $\mathrm{X} = \mathrm{S}$ or R represents RIS or the Rx_0, and $\mathrm{Y} = \mathrm{R}$ or T_i represents the the Rx_0 or the i-th Tx. The distance between X and Y is denoted by d while f is the transmission frequency. The geometric channel related to the LOS component is denoted by $\mathbf{f}_{\mathrm{LOS}}$ (or $\mathbf{F}_{\mathrm{LOS}}$) and the scattering counterpart is denoted by $\tilde{\mathbf{h}}_{\mathrm{XY}}$ (or $\tilde{\mathbf{H}}_{\mathrm{XY}}$) which is a complex vector (or matrix) with each entry being an independent and identically distributed (i.i.d.) complex normal random variable with zero mean and unit variance. Note that, when $\zeta = 1$, the scattering component vanishes and $\frac{K_d}{K_d+1} = \tau(f, d)$ corresponds to the transmittance, as expected. The distances and fixed channels associated with the different combinations of X and Y in the system model are compiled in Table I. We define the following stacked channels for notational ease:

$$\mathbf{Z}_i = \mathbf{H}_{\mathrm{SR}}\mathrm{diag}\left(\mathbf{h}_{\mathrm{ST}_i}\right), \quad \mathbf{H}_i = [\mathbf{Z}_i \ \mathcal{I}_i\mathbf{h}_{\mathrm{RT}_i}], \ \forall i \in [0, N_I], \quad (6)$$

where $\mathcal{I}_i$ is an indicator function that either takes 0 or 1 depending on the visibility of the direct link with probability P_{L_i}.

B. Imperfect CSI Model

In practical wireless systems, estimating wireless channels is crucial for establishing reliable communication links. Estimating non-cooperative interferer channels, however, is particularly difficult and prone to errors. A typical passive RIS cannot estimate individual channels (Tx-RIS and RIS-Rx). To overcome this, the cascaded channels, as shown in Eq. (6) in our work, are often estimated. The Rx usually estimates these cascaded channels using training pilot signals and RIS-associated training phase-shifts [42]. However, here we are abstracting the channel estimation procedure with an additive estimation error model [43], [44] to model this imperfect reflected channel as follows: $\mathbf{Z}_i = \hat{\mathbf{Z}}_i + \boldsymbol{\Delta}_i$, where the true channel is $\mathbf{Z}_i$, the estimated channel is $\hat{\mathbf{Z}}_i$, and the elements of the error matrix $\boldsymbol{\Delta}_i$ are i.i.d. as $\mathcal{CN}(0, \rho_i^2)$. Similarly, the error vector for the imperfect direct channel is $\boldsymbol{\delta}_i$ whose every element is i.i.d as $\mathcal{CN}(0, \rho_i'^2)$. The i.i.d. modeling implies a diagonal error covariance matrix, which can result from methods like least-squares channel estimation using orthogonal training sequences [45]. The imperfect direct channel is expressed as follows: $\mathbf{h}_{\mathrm{RT}_i} = \hat{\mathbf{h}}_{\mathrm{RT}_i} + \boldsymbol{\delta}_i$. Now, estimated stacked channels are defined as: $\hat{\mathbf{H}}_i = [\hat{\mathbf{Z}}_i \ \mathcal{I}_i\hat{\mathbf{h}}_{\mathrm{RT}_i}], \ \forall i \in [0, N_I]$. We consider $\{\rho_i, \rho_i'\}$ to be parameters in our model that control the extent of the uncertainty in our channel estimates. Note that the channel is perfect when these parameters are set to zero. Larger values of these parameters denote worse CSI quality.

C. Signal Model

If the signal x_i of power $\mathrm{E}[|x_i|^2] = P_i$ is transmitted by the i-th Tx, the received signal at Rx_0 is expressed as (7):

$$\begin{aligned}\mathbf{y} =& (\mathbf{h}_{\mathrm{RT}_0} + \mathbf{H}_{\mathrm{SR}}\mathrm{diag}\left(\mathbf{h}_{\mathrm{ST}_0}\right)\boldsymbol{\theta})x_0 + \\ & \sum_{i=1}^{N_I}(\mathbf{h}_{\mathrm{RT}_i} + \mathbf{H}_{\mathrm{SR}}\mathrm{diag}\left(\mathbf{h}_{\mathrm{ST}_i}\right)\boldsymbol{\theta})x_i + \mathbf{w}, \end{aligned} \quad (7)$$

where $\boldsymbol{\theta} = [e^{j\varphi_1} \ \dots \ e^{j\varphi_N}]^T$ is the RIS configuration vector, $\varphi_n \in [0, 2\pi]$ is the n-th entry of the vector $\boldsymbol{\varphi}$ for all $n \in \{1, \dots, N\}$ and denotes the n-th element's reflection coefficient, and $\mathbf{w}$ denotes the additive Gaussian noise with variance $\sigma_w^2 + \zeta\sigma_m^2$. The variance terms σ_w^2 and $\zeta\sigma_m^2$ represent the thermal noise and molecular re-radiation noise, respectively. Molecular re-radiation noise under Assumption 1 can be calculated as: $\sigma_m^2 = \sum_{i=0}^{N_I}\sigma_{m,i}^2$, where $\sigma_{m,i}^2$ is the molecular re-radiation noise due to the i-th Tx. Note that, as this $\zeta = 0$

XY	RT_i	ST_i	SR
d	d_i	d_{γ_i}	d_α
$\mathbf{f}_{\mathrm{LOS}}$ or $\mathbf{F}_{\mathrm{LOS}}$	$\mathbf{a}_{N_R}^H(\varphi_{R,i},\theta_{R,i},\mathbf{U}_{BS})$	$\mathbf{a}_N^H(\varphi_{S,i},\theta_{S,i},\mathbf{U}_{RIS})$	$\mathbf{a}_{N_R}^H(\varphi_\alpha,\theta_\alpha,\mathbf{U}_{BS})\times\mathbf{a}_N(\varphi_\beta,\theta_\beta,\mathbf{U}_{RIS})$

TABLE I: Channel Notations.

conforms to Assumption 2, the molecular re-radiation noise variance disappears and manifests as fading.

Now, we have all the information to make the signal model more compact with the stacked channel structure (6). Using that, the received signal is rewritten as:

$$\mathbf{y}=\mathbf{H}_0\boldsymbol{\theta}_0x_0+\sum_{i=1}^{N_I}\mathbf{H}_i\boldsymbol{\theta}_0x_i+\mathbf{w}, \tag{8}$$

where $\boldsymbol{\theta}_0=[\boldsymbol{\theta}^T\ 1]^T$. Now, we multiply the received signal with the receive beamformer $\mathbf{u}^H$ from the left and express the resulting received signal as:

$$\mathbf{u}^H\mathbf{y}=\mathbf{u}^H\hat{\mathbf{H}}_0\boldsymbol{\theta}_0x_0+\mathbf{u}^H\sum_{i=1}^{N_I}\hat{\mathbf{H}}_i\boldsymbol{\theta}_0x_i+\mathbf{u}^H\sum_{i=0}^{N_I}\left(\boldsymbol{\Delta}_i\boldsymbol{\theta}+\mathcal{I}_i\boldsymbol{\delta}_i\right)x_i+\mathbf{u}^H\mathbf{w}. \tag{9}$$

Here we inherently assume that the devices are capable of digital beamforming. However, this is a reasonable assumption due to the recent advances in THz communication. For example, Samsung recently demonstrated a fully digital solution with 128-element antenna arrays in the 140 GHz band [46]. While the first term in (9) represents our desired signal, the last three terms denote interference, channel estimation errors, and noise, respectively. As the exact channel capacity is unknown for the interference channel, we provide a well-known lower bound on the channel capacity C_{sys} based on the discrete memoryless interference channel [32, Corollary 1.3]:

$$C_{\mathrm{sys}}\geq\log_2\left(1+\gamma(\mathbf{u},\boldsymbol{\varphi})\right), \tag{10}$$

such that the SINR term $\gamma(\mathbf{u},\boldsymbol{\varphi})$ can be expressed as follows:

$$\gamma(\mathbf{u},\boldsymbol{\varphi})=\frac{P_0|\mathbf{u}^H\hat{\mathbf{H}}_0\boldsymbol{\theta}_0|^2}{\sum\limits_{i=1}^{N_I}P_i|\mathbf{u}^H\hat{\mathbf{H}}_i\boldsymbol{\theta}_0|^2+\sum\limits_{i=0}^{N_I}P_i\mathbf{u}^H\mathbf{C}_{e_i}\mathbf{u}+\sigma_w^2+\zeta\sigma_m^2}, \tag{11}$$

where $\{\mathbf{C}_{e_i}\}$ are the co-variance matrices for the estimation errors and can be calculated as follows:

$$\begin{aligned}\mathbf{C}_{e_i}&=\mathrm{E}\Big[(\boldsymbol{\Delta}_i\boldsymbol{\theta}+\mathcal{I}_i\boldsymbol{\delta}_i)(\boldsymbol{\Delta}_i\boldsymbol{\theta}+\mathcal{I}_i\boldsymbol{\delta}_i)^H\Big]\\&\overset{(a)}{=}\mathrm{E}\Big[\boldsymbol{\Delta}_i\boldsymbol{\theta}\boldsymbol{\theta}^H\boldsymbol{\Delta}_i^H\Big]+\mathcal{I}_i\mathrm{E}\Big[\boldsymbol{\delta}_i\boldsymbol{\delta}_i^H\Big]\overset{(b)}{=}(N\rho_i^2+\mathcal{I}_i\rho_i'^2)\mathbf{I}_{N_R},\end{aligned} \tag{12}$$

where (a) follows from the fact that the errors are uncorrelated, and (b) follows from using the identity $\mathrm{E}\left[\boldsymbol{\Delta}_i\boldsymbol{\theta}\boldsymbol{\theta}^H\boldsymbol{\Delta}_i^H\right]=\rho_i^2\mathrm{Tr}\left(\boldsymbol{\theta}\boldsymbol{\theta}^H\right)\mathbf{I}_{N_R}$. Although the SINR expression (11) is a function of the RIS phase-shift vector $\boldsymbol{\varphi}$, the arguments and the optimization variable associated to the RIS might be functions of $\boldsymbol{\varphi}$ in the later formulations depending on the context of the specific optimization problem later constructed.

Lemma 1. *In Assumption I, the re-radiated signal from the* Tx_i *is modeled as additive Gaussian noise with variance* $\zeta\sigma_{m,i}^2$ *for the* Tx_i*, where* $\sigma_{m,i}^2=\mathcal{I}_i\sigma_{m_1,i}^2+N\sigma_{m_2,i}^2$ *with* $\sigma_{m_1,i}^2=\left(\frac{c}{4\pi fd_i}\right)^2P_i[1-\tau(f,d_i)]$ *and* $\sigma_{m_2,i}^2=\left(\frac{c^2}{16(\pi f)^2}\frac{1}{d_\alpha d_{\gamma_i}}\right)^2P_i[1-\tau(f,d_\alpha)\tau(f,d_{\gamma_i})]$.

Proof: See Appendix A. ∎

We define $\sigma_{m_1}^2=\sum\limits_{i=0}^{N_I}\mathcal{I}_i\sigma_{m_1,i}^2$ and $\sigma_{m_2}^2=\sum\limits_{i=0}^{N_I}\sigma_{m_2,i}^2$ using Lemma 1 for convenient notation. This completes the SINR (11) description. Estimating the noise variance necessitates explicit knowledge of both path-loss and the molecular absorption coefficient at the operating frequency. The noise variance plays a crucial role in the objective function of the optimization problem, affecting the solution while preserving the overall structure of the problem, as illustrated in the next section.

III. Robust Optimization of Receive Beamformer and RIS Configuration Vector

In this section, we jointly optimize the receive beamforming weights and the RIS configuration vector. We assume that Rx_0 knows the estimation error variances in the robust case. As the exact channel capacity is not computable, we set the objective function as a well-known lower bound of the channel capacity (10) under imperfect CSI. Maximizing a lower bound is useful in its own right as it effectively maximizes the channel capacity. However, maximizing $\log_2\left(1+\gamma(\mathbf{u},\boldsymbol{\varphi})\right)$ is equivalent to maximizing $\gamma(\mathbf{u},\boldsymbol{\varphi})$ due to the monotonically increasing nature of logarithm function. The new objective function (11) is non-convex due to the coupling between the two sets of variables. The non-convex constraint of unit modulus makes the problem more difficult. We employ the BCD method to solve this optimization problem by separating it into two sub-problems, one for each set of variables, and solving each sub-problem in an alternating manner, to obtain an efficient solution. With a fixed RIS phase vector, the receive beamformer sub-problem can be conveniently posed as a maximization of a Rayleigh quotient problem, and hence has a simple analytical solution. However, the RIS sub-problem does not have an analytical solution. We propose three methods of different complexities to achieve suboptimal solutions: a) SDP with Gaussian randomization, b) SA, and c) GD approach. Finally, we show the convergence and compare the complexities of the proposed algorithms.

A. Problem Formulation

Our objective is to maximize the effective SINR of Tx_0 given the estimated channel such that the norm of receive beamforming vector is unity, and the RIS elements follow unit modulus constraint. The transmit power P_0 of the user is set

as the maximum allowable power to maximize the objective. Now, the optimization problem can be formulated as:

$$\max_{\mathbf{u},\boldsymbol{\varphi}} \quad \gamma(\mathbf{u},\boldsymbol{\varphi}) \tag{13a}$$
$$\text{s.t.} \quad \|\mathbf{u}\|_2^2 = 1, \tag{13b}$$
$$0 \leq \varphi_n < 2\pi, \quad \forall n = 1,2,\ldots,N. \tag{13c}$$

The general BCD algorithm used for the optimization here is shown in Algorithm 3. Note that under imperfect CSI, initializing the $\{\rho_i, \rho_i'\}$ to zero results in the non-robust counterpart of this algorithm. The non-robust algorithm treats the estimated CSI as the perfect instantaneous CSI and is used as a benchmark for the performance of the robust algorithms.

B. Receive Beamformer Optimization

As noted before, for a given $\boldsymbol{\theta}$, this sub-problem can be expressed as an unconstrained maximization of a Rayleigh quotient:

$$\max_{\mathbf{u}} \quad \frac{\mathbf{u}^H \mathbf{B}_0 \mathbf{u}}{\mathbf{u}^H \left(\sum_{i=1}^{N_I} P_i \mathbf{B}_i + (\rho_{\text{total}} + \sigma_w^2 + \zeta\sigma_m^2)\mathbf{I}_{N_R} \right) \mathbf{u}},$$
$$\text{s.t.} \quad \|\mathbf{u}\|_2^2 = 1, \tag{14}$$

where $\rho_{\text{total}} = \sum_{j=0}^{N_I} P_j(N\rho_j^2 + \mathcal{I}_j\rho_j'^2)$, $\mathbf{B}_i = \hat{\mathbf{H}}_i \boldsymbol{\Psi} \hat{\mathbf{H}}_i^H$, and $\boldsymbol{\Psi} = \boldsymbol{\theta}_0 \boldsymbol{\theta}_0^H$. The normalized analytical solution for the given problem is given by [47]:

$$\mathbf{u}^* = \frac{\left(\sum_{i=1}^{N_I} P_i \mathbf{B}_i + (\rho_{\text{total}} + \sigma_w^2 + \zeta\sigma_m^2)\mathbf{I}_{N_R} \right)^{-1} \mathbf{e}_0}{\left\| \left(\sum_{i=1}^{N_I} P_i \mathbf{B}_i + (\rho_{\text{total}} + \sigma_w^2 + \zeta\sigma_m^2)\mathbf{I}_{N_R} \right)^{-1} \mathbf{e}_0 \right\|}, \tag{15}$$

where $\mathbf{e}_0 = \hat{\mathbf{H}}_0 \boldsymbol{\theta}_0$ is the dominant eigenvector of $\mathbf{B}_0$ and the solution is normalized to ensure a unit norm vector.

C. RIS Optimization through SDP

We approach this sub-problem through SDP as it provides an efficient near-optimal solution by relaxing the original non-convex sub-problem to a convex optimization problem. To that end, we express (11) for a given receive beamformer $\mathbf{u}$ as:

$$\gamma(\mathbf{u},\boldsymbol{\Psi}) = \frac{\boldsymbol{\theta}_0^H \mathbf{G}_0 \boldsymbol{\theta}_0}{\boldsymbol{\theta}_0^H \mathbf{M} \boldsymbol{\theta}_0 + \alpha} \overset{(a)}{=} \frac{\text{Tr}(\boldsymbol{\Psi}\mathbf{G}_0)}{\text{Tr}(\boldsymbol{\Psi}\mathbf{M}) + \alpha}, \tag{16}$$

where $\mathbf{G}_i = P_i \hat{\mathbf{H}}_i^H \mathbf{U} \hat{\mathbf{H}}_i$, $\mathbf{M} = \sum_{i=1}^{N_I} \mathbf{G}_i + \frac{\rho_{\text{total}}}{N}\mathbf{I}_{N+1} + \zeta\sigma_{m_2}^2 \mathbf{I}_{N+1}$, $\alpha = \sigma_w^2 + \zeta(\sigma_{m_1}^2 - \sigma_{m_2}^2) - \frac{\rho_{\text{total}}}{N}$, $\mathbf{U} = \mathbf{u}\mathbf{u}^H$, and (a) follows from utilizing trace operator and rearranging the terms. This reformulation imposes a positive semidefiniteness and a rank constraint on $\boldsymbol{\Psi}$. Unlike the first constraint, the second rank constraint that rank($\boldsymbol{\Psi}$) should be unity is non-convex. Relaxing this constraint is termed as SDR. The sub-problem with SDR is expressed as follows:

$$\max_{\boldsymbol{\Psi}} \quad \frac{\text{Tr}(\boldsymbol{\Psi}\mathbf{G}_0)}{\text{Tr}(\boldsymbol{\Psi}\mathbf{M}) + \alpha},$$
$$\text{s.t.} \quad \boldsymbol{\Psi} \succeq 0,$$
$$[\boldsymbol{\Psi}]_{l,l} = 1, \quad \forall l = 1,2,\ldots,N+1. \tag{17}$$

Following [48], we introduce an auxiliary variable $b \geq 0$ to transform (17) to an epigraph form:

$$\gamma^* = \max_{\boldsymbol{\Psi}, b \geq 0} \quad b$$
$$\text{s.t.} \quad \text{Tr}(\boldsymbol{\Psi}\mathbf{G}_0) \geq b\text{Tr}(\boldsymbol{\Psi}\mathbf{M}) + b\alpha,$$
$$\boldsymbol{\Psi} \succeq 0,$$
$$[\boldsymbol{\Psi}]_{l,l} = 1, \quad \forall l = 1,2,\ldots,N+1. \tag{18}$$

With $b \geq 0$, the inherent feasibility problem is:

$$\text{Find} \quad \boldsymbol{\Psi}$$
$$\text{s.t.} \quad \text{Tr}(\boldsymbol{\Psi}\mathbf{G}_0) \geq b\text{Tr}(\boldsymbol{\Psi}\mathbf{M}) + b\alpha,$$
$$\boldsymbol{\Psi} \succeq 0,$$
$$[\boldsymbol{\Psi}]_{l,l} = 1, \quad \forall l = 1,2,\ldots,N+1. \tag{19}$$

Note that if the above problem is feasible then $\gamma(\mathbf{u},\boldsymbol{\Psi})^* \geq b$, while the opposite condition $\gamma^*(\mathbf{u},\boldsymbol{\Psi}) \leq b$ holds when the above problem is infeasible. So, using bisection for (19) provides a good solution for $\boldsymbol{\Psi}$. The problem (19) can be solved by any standard convex optimization package like CVX [49], [50]. However, this solution will generally not be a rank-one solution. We extract a rank-one solution by Gaussian randomization [48], as discussed next. The unit circle projection (the division of each entry of the vector by its absolute value) of the rank-one solution provides $\boldsymbol{\theta}^*$.

Algorithm 1: BCD-SDR

Input: $\mathbf{G}_0, \mathbf{M}, \alpha, G, \mathbf{u}_{q+1}$
Output: $\bar{\boldsymbol{\theta}}_{q+1}$
Obtain $\boldsymbol{\Psi}_{q+1}$ by using bisection on (19).
Generate G feasible solutions for $\bar{\boldsymbol{\theta}}_{0_{q+1}}$ through Gaussian randomization [48].
Choose the solution with unit circle projection $\bar{\boldsymbol{\theta}}_{q+1}$ that provides the highest $\gamma_{q+1} = \gamma(\mathbf{u}_{q+1}, \bar{\boldsymbol{\theta}}_{q+1})$ through (11).

Gaussian Randomization: The Gaussian randomization scheme [51] entails generation of a random vector $\mathbf{z} \sim \mathcal{CN}(\mathbf{0}_{N+1}, \vartheta)$ where ϑ is the Cholesky decomposition of $\boldsymbol{\Psi}$ to extract a rank-one solution. The rank-one candidate for one such vector is $\left[\frac{\mathbf{z}_N^T}{\|\mathbf{z}_N\|} \; 1\right]^T$, where $\mathbf{z}_N$ is the vector consisting of the first N elements of $\mathbf{z}$. A number of such candidates are generated to choose the one that is feasible and provides the largest objective value among them. The approximation accuracy of such a scheme in different scenarios is well-investigated by [51]. The worst-case approximation accuracy was proved to be reasonable for a finite number of generations. However, the complexity of this problem is prohibitive for RISs with large number of elements [31]. This encourages us to explore some low-complexity approaches in the subsequent subsections.

D. SA Solution to the RIS Sub-problem

A low-complexity approach to the RIS sub-problem is to maximize the received signal strength as opposed to SINR

due to the existence of a closed-form solution [15]. As this approach aligns the phases of reflected signal with the phase of the direct signal, we denote this approach as SA and is:

$$\boldsymbol{\theta}_i = e^{-j\left(\arg(\mathbf{u}^H\hat{\mathbf{Z}}_0)_i - \arg(\mathbf{u}^H\hat{\mathbf{h}}_{\mathrm{RT}_0})\right)}. \tag{20}$$

This can incur some performance loss from the global optimum solution. Since most RIS phase-shift optimization problems are NP-hard, a global optimum is difficult to obtain [52]. However, it has been demonstrated that the local optimal solutions can improve performance significantly [19], [20]. In that case, the performance loss can be characterized by finding good stationary points. In [19], a stationary point of a general SINR is found with respect to the phase-shift of one element without considering direct links to facilitate the element-wise BCD algorithm. Meanwhile, the authors of [18] obtain a stationary point of an SINR expression in an N-element active RIS-aided network that does not consider interference. This was possible as the active RIS elements do not have the unit modulus constraint of passive RIS. However, a similar analysis has not been done for the passive RIS. To fill this gap, we provide an analysis next for a one-element passive RIS with only one interferer while considering direct links.

One-element RIS Sub-problem: A generic SINR expression for an one-element RIS with only one interferer can be readily written as:

$$\gamma_{oe} = \frac{P_0|a_1\theta_1 + h|^2}{P_1|b_1\theta_1 + g|^2 + c} = \frac{L' + M'\cos(s+x)}{N' + P'\cos(t+x)}, \tag{21}$$

where $a_1, b_1, \theta_1,$ and c denote the reflected signal channel, reflected interferer channel, RIS phase-shifts and noise. The direct signal and interferer channels are denoted by h and g, respectively. However, we will use the second form to derive the stationary points where $L' = P_0(|a_1|^2 + |h|^2), M' = 2P_0|a_1||h|, N' = P_1(|b_1|^2 + |g|^2) + c, P' = 2P_1|b_1||g|, s = \angle a_1 - \angle h, t = \angle b_1 - \angle g$, and $x = \angle\theta_1$.

Theorem 1. *The SINR for one-element RIS takes one of the two values at the stationary points given by:*

$$\gamma^*_{oe} = \frac{L'}{N'} - \frac{1}{N'}\frac{C'}{\Big(P'(L'P' - M'N'\cos(s-t)) \pm N'\sqrt{C' - (M'P'\sin(s-t))^2}\Big)}, \tag{22}$$

where $C' = (L'P')^2 + (M'N')^2 - 2L'M'N'P'\cos(s-t)$.

Proof: See Appendix B. ∎

Remark 2. *In the simple setting without interference or $P_1 \to 0$, the SINR $\gamma^*_1 \to \frac{L'+M'}{N'}$. This is a result of choosing θ_1 in a way to align the phase of $a_1\theta_1$ with h, which is the SA method. In absence of interference, the optimal solution is the SA solution.*

Corollary 1. *In a simple setting where $|a_1|, |b_1|, |h|, P_1, P_0$ are unity and $|g| = k$, the SINR for the SA solution is $g_1(k) = \frac{16k^2\sin^2(s-t)}{(k^2+2k\cos(s-t)+1+c)((k+1)^2+c)((k-1)^2+c)}$ below the higher stationary point and $g_2(k) = \frac{4}{k^2+2k\cos(s-t)+1+c}$ above the lower stationary point.*

Proof: The SA solution in this case is $x = -s$. The resulting SINR is denoted by $\gamma^h_2 = \frac{L'+M'}{N'+P'\cos(s-t)}$. Both $g_1(k)$ and $g_2(k)$ can be calculated easily by evaluating $|\gamma^*_1 - \gamma^h_2|$. ∎

Remark 3. *Note that $g_1(k)$ and $g_2(k)$ both tend to zero when $k \to \infty$. In other words, the stationary points converge to the SA solution when the interferer direct link is too powerful. In a practical scenario, where the interferer direct link is as powerful as the reflected link or $k \to 1$, $g_1(k) \to \frac{16\sin^2(s-t)}{(4c+c^2)(2\cos(s-t)+2+c)}$ implying the sub-optimality of the SA solution.*

The findings from the single-element RIS analysis suggest that, for a multi-element RIS, the quality of the SA solution deteriorates further due to the presence of more stationary points when increasing the problem's dimension. This analytical validation encourages us to devise a low-complexity algorithm that outperforms the SA in providing a superior solution.

E. Gradient Descent Approach to the RIS Sub-problem

Achieving a better solution than the SA method while retaining its low-complexity benefit requires a different approach. As noted in the previous subsection, local optimal solutions can provide significant performance improvement. Gradient descent is a natural choice for such a solution because it tries to converge to a local minimum from the initial point in the chosen descent direction. Generally, the chosen descent direction is the steepest one or the negative gradient of the objective function. As shown next, this can be calculated from an alternate formulation of our RIS sub-problem in an unconstrained manner with respect to $\boldsymbol{\varphi} = [\varphi_1 \ \dots \ \varphi_n]^T$:

$$\min_{\boldsymbol{\varphi}} \quad -\frac{\boldsymbol{\theta}^H\mathbf{R}_0\boldsymbol{\theta} + 2\mathrm{Re}(\mathbf{c_0}\boldsymbol{\theta})}{\boldsymbol{\theta}^H\mathbf{K}\boldsymbol{\theta} + 2\mathrm{Re}(\mathbf{z}\boldsymbol{\theta})}, \tag{23}$$

where $\mathbf{R}_i = P_i\left(\hat{\mathbf{Z}}_i^H\mathbf{U}\hat{\mathbf{Z}}_i + \frac{|\mathcal{I}_i\mathbf{u}^H\hat{\mathbf{h}}_{\mathrm{RT}_i}|^2}{N}\mathbf{I}_N\right), \mathbf{K} = \sum_{i=1}^{N_I}\mathbf{R}_i + \left(\frac{\rho_{\mathrm{total}}+\sigma_w^2+\zeta\sigma_{m_1}^2}{N} + \zeta\sigma_{m_2}^2\right)\mathbf{I}_N$, $\mathbf{c}_i = P_i\mathcal{I}_i\hat{\mathbf{h}}^H_{\mathrm{RT}_i}\mathbf{u}\mathbf{u}^H\hat{\mathbf{Z}}_i$, and $\mathbf{z} = \sum_{i=1}^{N_I}\mathbf{c}_i$. The gradient can be calculated as follows:

$$\nabla_{\boldsymbol{\varphi}}(\boldsymbol{\varphi}) = 2\mathrm{Re}\left\{\frac{(\mathbf{R}_0^*\boldsymbol{\theta}^* + \mathbf{c}_0^T)\odot(-j\boldsymbol{\theta})}{\boldsymbol{\theta}^H\mathbf{K}\boldsymbol{\theta} + 2\mathrm{Re}(\mathbf{z}\boldsymbol{\theta})} + \frac{\left(\boldsymbol{\theta}^H\mathbf{R}_0\boldsymbol{\theta} + 2\mathrm{Re}(\mathbf{c_0}\boldsymbol{\theta})\right)\cdot(\mathbf{K}^*\boldsymbol{\theta}^* + \mathbf{z}^T)\odot(j\boldsymbol{\theta})}{\left(\boldsymbol{\theta}^H\mathbf{K}\boldsymbol{\theta} + 2\mathrm{Re}(\mathbf{z}\boldsymbol{\theta})\right)^2}\right\}. \tag{24}$$

Remark 4. *By substituting $\{\mathbf{C}_i\}$ as zero vectors, we obtain the same objective function and the gradient as [31].*

Armed with the analytical expression of the gradient, a simple GD algorithm works through the simple update rule: $\boldsymbol{\varphi}^{(t+1)} = \boldsymbol{\varphi}^{(t)} - \beta^{(t)}\boldsymbol{\nabla}_{\boldsymbol{\varphi}}\left(\boldsymbol{\varphi}^{(t)}\right)$, where $\boldsymbol{\varphi}^{(t)}$ is the RIS phase vector at t-th iteration, $\beta^{(t)}$ is the step-size and $\boldsymbol{\nabla}_{\boldsymbol{\varphi}}\left(\boldsymbol{\varphi}^{(t)}\right)$ is the gradient. The convergence time depends on choosing an appropriate step-size. Improper step-size can cause slow

convergence due to oscillation or slow descent. Backtracking line searches offer a practical solution, starting with an initial step-size and diminishing it iteratively to ensure a sufficient decrease in the descent direction. Moreover, [53] shows that GD with diminishing step sizes almost always avoids saddle points under random initialization. It is also shown in [54] that saddle points can slow down GD with constant step size considerably to the extent of needing exponential time to escape, even with random initialization schemes. The objective function is highly non-convex and expected to have multiple saddle points, so being able to avoid saddle points is a desirable property. With these motivating factors, we choose Armijo-Goldstein (AG) line search [55]. This strategy ensures that $\beta^{(t)}$ satisfies $-\gamma\left(\mathbf{u}, \boldsymbol{\varphi}^{(t)} - \beta^{(t)}\boldsymbol{\nabla}_{\boldsymbol{\varphi}}\left(\boldsymbol{\varphi}^{(t)}\right)\right) \leq -\gamma\left(\mathbf{u}, \boldsymbol{\varphi}^{(t)}\right) - \varepsilon\beta^{(t)}\|\boldsymbol{\nabla}_{\boldsymbol{\varphi}}\left(\boldsymbol{\varphi}^{(t)}\right)\|_2^2$, where $0 < \varepsilon < 1$ is a constant. If this condition is violated, the step-size is decreased by a factor of $0 < \varrho < 1$ starting from a larger initial step-size. Complete details of the GD approach are shown in Algorithm 2. Our proposed algorithm uses the SA solution as the initial point. With all the sub-problem solutions, the general BCD framework is demonstrated in Algorithm 3.

Algorithm 2: BCD-GD

Input: $\mathbf{L}_0, \mathbf{Z}, \varrho, \varepsilon, \epsilon_{th}, \beta_0, \mathbf{u}_{q+1}$
Output: $\bar{\boldsymbol{\theta}}_{q+1}$
Initialize $t = 1$, $\delta_{GD} = 1$, and
$\boldsymbol{\varphi}^{(t)} = -\arg(\mathbf{u}_{q+1}^H \mathbf{H}_0)_i$.
while $\delta_{GD} \leq \epsilon_{th}$
do
  Initialize $\beta^{(1)} = \beta_0$.
  Calculate $\boldsymbol{\nabla}_{\boldsymbol{\varphi}}\left(\boldsymbol{\varphi}^{(t-1)}\right)$ from (24).
  while $-\gamma\left(\mathbf{u}_{q+1}, \boldsymbol{\varphi}^{(t)} - \beta^{(t)}\boldsymbol{\nabla}_{\boldsymbol{\varphi}}\left(\boldsymbol{\varphi}^{(t)}\right)\right) \geq -\gamma\left(\mathbf{u}_{q+1}, \boldsymbol{\varphi}^{(t)}\right) - \varepsilon\beta^{(t)}\|\boldsymbol{\nabla}_{\boldsymbol{\varphi}}\left(\boldsymbol{\varphi}^{(t)}\right)\|_2^2$
  do
    $\beta^{(t)} = \varrho\beta^{(t)}$.
  end
  $\delta_{GD} = \beta^{(t)}\|\boldsymbol{\nabla}_{\boldsymbol{\varphi}}\left(\boldsymbol{\varphi}^{(t)}\right)\|_2^2$.
  $\boldsymbol{\varphi}^{(t+1)} = \boldsymbol{\varphi}^{(t)} - \beta^{(t)}\boldsymbol{\nabla}_{\boldsymbol{\varphi}}\left(\boldsymbol{\varphi}^{(t)}\right)$.
  $t = t + 1$.
end
$\bar{\boldsymbol{\theta}}_{q+1} = \exp(-j\boldsymbol{\varphi}^{(t)})$.

Algorithm 3: Joint Optimization by BCD

Input: $\mathbf{H}_i, \zeta, \epsilon\ \forall i$
Output: $\boldsymbol{\theta}^*, \mathbf{u}^*$
Initialize $\bar{\boldsymbol{\theta}}_q$ with a random vector, $q = 0$, $\gamma_0 = 0$, and $\Delta = \epsilon + 1$.
while $\Delta > \epsilon$ **do**
  Obtain $\mathbf{u}_{q+1}$ from (15).
  Obtain $\bar{\boldsymbol{\theta}}_{q+1}$ from Algorithm 1, 2 or (20).
  Calculate $\gamma_{q+1} = \gamma(\mathbf{u}_{q+1}, \boldsymbol{\theta}_{q+1})$ from (11).
  if $\gamma_{q+1} \leq \gamma_q$ **then**
    Set $\bar{\boldsymbol{\theta}}_{q+1} = \bar{\boldsymbol{\theta}}_q$ to keep the objective value non-decreasing.
  end
  Evaluate $\Delta = |\gamma_{q+1} - \gamma_q|/\gamma_q$.
  $q = q + 1$.
end
$\boldsymbol{\theta}^* = \bar{\boldsymbol{\theta}}_{q-1}$.

F. Convergence and Complexity Discussion

The BCD algorithm presented in Algorithm 3 ensures non-decreasing objective values after each iteration. As the objective function is also upper bounded by some value, Algorithm 3 converges regardless of the approach taken to solve the RIS sub-problem. However, all the approaches are of varying complexities. In this subsection, worst-time complexities are derived in the big-O notation for the algorithms when tractable and run-times are compared numerically. First, for each iteration of the BCD algorithm, we will calculate the time complexity for each sub-problem.

1) Beam-former Optimization: The total complexity of the calculation of each $\mathbf{B}_i$ for all $i = 0, 2 \ldots, N_I$ is $O(N_R^2 N(N_I + 1))$. The multiplication with $\mathbf{e}_0$, the inverse, and the norm operation have time complexities of $O(N_R^2), O(N_R^3)$, and $O(N_R)$, respectively. So, the total time complexity is $O((N_R^2 N(N_I + 1) + N_R^3 + N_R^2 + N_R) = O(N_R^2 N(N_I + 1) + N_R^3)$.

2) SDR Algorithm: First, the calculation of $N_I + 1$ $\{\mathbf{G}_i\}$ has a time complexity of $O(((N + 1)N_R + (N + 1)^2)(N_I + 1)) = O(N(N_I + 1)(N + N_R))$. The feasibility problem (19) is a classic semi-definite programming problem and is solved by interior-point method. The worst time complexity is $O((N + 1)^{4.5})$ [56], [57]. This computation happens every iteration of the bisection algorithm. The number of iterations needed is $\log_2\left(\frac{\epsilon_0}{\epsilon_1}\right)$, where ϵ_0 and ϵ_1 denote the upper bound and the tolerance for the bisection problem, respectively [58]. So, the worst-case time complexity of the feasibility problem (19) with the bisection procedure and the matrix multiplications is $O\Big(N(N_I + 1)(N + N_R) + (N + 1)^{4.5}\log_2\left(\frac{\epsilon_0}{\epsilon_1}\right)\Big) = O\Big(N(N_I + 1)(N + N_R) + N^{4.5}\log_2\left(\frac{\epsilon_0}{\epsilon_1}\right)\Big)$. For the Gaussian randomization procedure, we need to do a Cholesky factorization to create a normal random variable with the covariance matrix $\boldsymbol{\Psi}^*$ as per [48]. The time complexity of this operation is $O((N + 1)^3) = O(N^3)$. Next, the creation of G number of random samples requires a time complexity of $O(G(N + 1)^2) = O(GN^2)$. Finally adding both of them together and ignoring lower order terms, the SDR algorithm has a time complexity of $O\left(N^{4.5}\log_2\left(\frac{\epsilon_0}{\epsilon_1}\right) + N^3 + N(N_I + 1)(N + N_R) + GN^2\right)$.

3) SA Solution: The SA solution has a time complexity of $O(N_R^2 N)$ resulting from the multiplication between $\mathbf{u}^H$ and $\mathbf{H}_0$.

4) GD Algorithm: The complexity of this method is dominated by the gradient and initial point calculation. Assuming I_1 iterations of the GD algorithm, one iteration of gradient calculation requires pre-calculating $\mathbf{R}_i$ and $\mathbf{c}_i$ for all $i = 0, 1, \ldots, N_I$ along with the calculation of the gradient expression. The former incurs a worst-time complexity of $O((N_I+1)(N^2+2N_R N))$ while the latter has a time complexity of $O(4N^2)$. Considering the initial point calculation, the total time complexity is $O(I_1((N_I+1)(N^2+2N_R N)+4N^2)+N_R^2 N)$. Now the run-times for one iteration at $(N_R = 100)$

RIS Sub-problem	Complexity	Runtime
BCD-SDR	$O(N^{4.5}\log_2\left(\frac{\epsilon_0}{\epsilon_1}\right) + N^3 + N(N_I+1)(N+N_R)+GN^2)$	129.4 sec
BCD-SA	$O(N_R^2 N)$	0.012 sec
BCD-GD	$O(I_1((N_I+1)(N^2+2N_R N)+4N^2)+N_R^2 N)$	0.005 sec

TABLE II: Complexity Comparison.

and $N = 100$ are compared in Fig. 2c and compiled in Table II along with the complexities. The algorithm with the SA sub-problem solution is denoted by BCD-SA.

IV. Numerical Results

In this section, we provide numerical results to quantify the impact of molecular re-radiation, RIS elements, Rx antennas, interferers, and channel estimation error on key performance metrics of an RIS-aided wireless network inspired by a 3D indoor xR setup. In the spherical coordinate system (r, φ, θ), with r in meters and angles defined in (1), the simulation setup places Rx_0, a square URA with 100 antennas, at the origin $(0, 0°, 0°)$ on the positive y-z plane. The RIS with 100 elements in a square URA pattern is situated 1m along the positive x-axis from Rx_0. The Tx_0 is placed at $(1, 60°, 0°)$ and transmits at 2 W (33 dBm) effective isotropic radiated power (EIRP) (which is within typical operating parameters of THz systems, e.g., see [59]) over a large bandwidth specified later. Therefore, we consider the Tx antenna gains $G_{Tx,i} = 1 \quad \forall i = 0, 1, ..., N_i$. The location of the interferer is $(1.5, 110°, 0°)$, and it transmits at the same power level. Note that these locations are chosen to ensure that all the nodes operate in a far-field region and in the 180° coverage zone of the RIS assumed to be installed on a wall. Unless otherwise specified, the system parameters for the simulation configuration are as follows: the transmission carrier frequency of 220 GHz, bandwidth of 10 GHz, relative humidity of 50%, standard atmospheric pressure of 1 atm, and temperature of 27°C. These parameters determine the value of $k(f)$. In addition, the thermal noise variance is assumed to be -174 dBm/Hz. For the general BCD algorithm, the parameter ϵ is 10^{-6}. The parameters ϵ_0, ϵ_1, and G in the SDR sub-problem are $20, 10^{-6}$, and 1000, respectively. The parameters $\varepsilon, \epsilon_{th}, \beta_0$, and ϱ in the GD sub-problem are $0.00005, 10^{-6}, 1$, and 0.5, respectively. We have used throughput and uncoded symbol error rate (SER) as the performance metrics. Throughput is calculated by the expression BC_{sys} for the perfect CSI case and throughput results are averaged over 2000 iterations. SER is calculated using 4-QAM modulation scheme and SER results are averaged over 10^6 symbols. We also assume that direct signal path is completely blocked to focus on the RIS's capability. This use-case focuses on indoor THz communications, where LoS link visibility depends on transmission frequency and the probability of self-blockage or dynamic blockage [7].

Legend notations: In the figures, the notations 'ND' and 'D' denote the two cases regarding the availability of the direct links of the interferers. In particular, 'ND' and 'D' correspond to $P_{L_i} = 0$ (*no direct link*), and $P_{L_i} = 1$ (*direct link*) for all $i = 1, 2, \ldots, N_I$, respectively. Similarly, the abbreviations 'N'

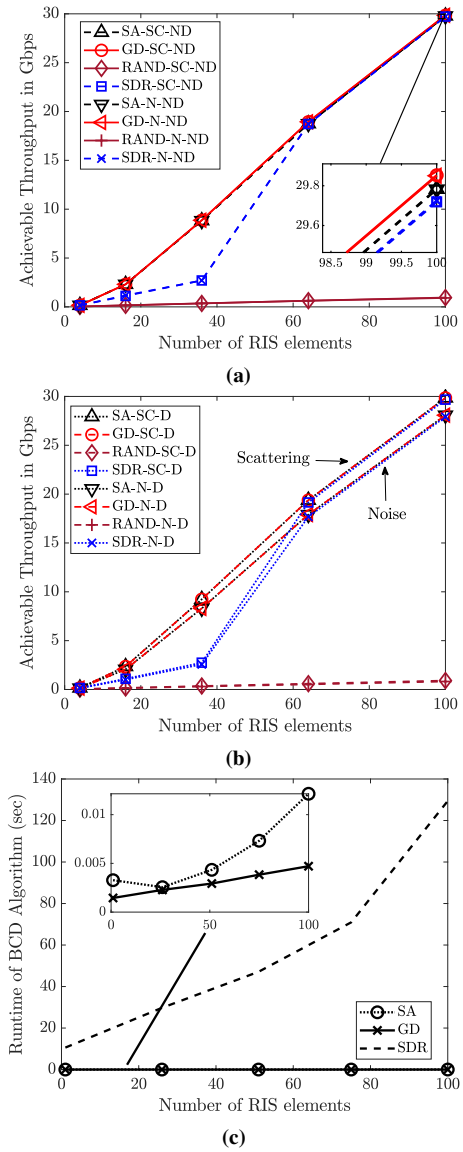

Fig. 2: Achievable throughput with the number of RIS elements when (a) Interferer direct links do not exist, (b) Interferer direct links exist, and (c) runtime in seconds with the number of RIS elements,

and 'SC' denote Assumptions 1 and 2, respectively. Additionally, the algorithms 'BCD-SA', 'BCD-GD' and 'BCD-SDR' are abbreviated as 'SA', 'GD' and 'SDR'. These algorithms are compared with random phase-shift RIS and optimized receive beamformer baseline performance denoted as 'RAND'. The robust and non-robust counterparts of the algorithms are denoted by 'R' and 'NR', respectively.

Runtime comparison of different algorithms: In Fig. 2c, we plot run-times of one iteration of the three different algorithms against different numbers of RIS elements. These run-times are averaged from the simulations needed to create Fig. 2a and 2b on a 3.59GHz AMD Ryzen 5 3600 6-Core PC with 16GB RAM. We observe that GD is the fastest algorithm while SDR is the slowest. The run-time of GD increases linearly, unlike SA and SDR, potentially because the GD sub-problem performs better in the BCD environment, providing a near-optimal solution instead of a guaranteed sub-optimal SA

solution.

Effect of Number of RIS elements on achievable throughput: In Fig. 2a and 2b, we plot achievable throughput for the perfect CSI case with varying numbers of RIS elements in the presence of a single interferer. The throughput increases nearly linearly with the number of RIS elements, resulting from large bandwidth in the low to moderate SINR regime ($0-7$ dB). In this regime, SINR is proportional to N^2, leading to an almost linear throughput increase.

The optimized system provides an increase of 30 Gbps throughput over the baseline at $N = 100$. The gap between assumptions is more visible in Fig. 2b where the interferer direct links are present due to the high re-radiation noise power from the interferer direct path that is absent in Fig. 2a. In Fig. 2b, Assumption 2 provides almost 2 Gbps of throughput increase from Assumption 1 when $N \in \{64, 100\}$. In Fig. 2a, the SA solution is near-optimal and almost overlaps with the GD and the SDR solutions due to low interference in accordance with Remark 2. However, in Fig. 2b, as the interferer direct link is much stronger than the reflected link (as a result of our chosen path-loss model and scenario), the stationary points converge to the SA solution following Remark 3. This behavior is verified by the overlap of the GD and SA solutions. From the zoomed plot in Fig. 2a, BCD-GD performs slightly better than both BCD-SA and BCD-SDR. However, the gap between BCD-GD and BCD-SA vanishes in Fig. 2b. In summary, BCD-SA and BCD-GD both achieve similar performance to the conventional BCD-SDR under perfect CSI while being fast. Next, we examine throughput as a function of Rx antennas with interferer direct links present, since the 'ND' scenario offers limited information on assumptions.

Effect of Rx antennas and estimation of ζ on achievable throughput: In Fig. 3a and 3b, we plot throughput versus number of Rx antennas. We investigate extreme mismatch cases mentioned in Remark 1 where optimization is based on Assumption 1 while Assumption 2 is true, and vice versa. This mismatch in the manifestation assumptions is the sole source of error. Our assumption for the optimization procedure only affects the amount of noise in the SINR expression. The cases of perfect and opposite ζ estimation are shown in Fig. 3a and 3b, respectively. Fig. 3 shows that joint optimization is not highly sensitive to model assumptions when the model mismatch is the only error source, as optimization differs mainly in noise amount. Furthermore, since the Rx points to the RIS due to a blocked signal direct link, it suppresses direct interference through sidelobe management, resulting in linear SINR scaling and logarithmic throughput scaling with Rx antennas N_R, unlike the near-linear throughput scaling seen with RIS elements.

Effect of CSI quality on SER: We plot SER versus CSI quality and number of interferers in Fig. 4 where we consider CSI quality of the signal link and the interferer links by defining $\sigma_0^2 = \eta_1^2 = \alpha_{\eta_1}^2 \|\text{vec}(\mathbf{H}_0)\|^2$, and $\sigma_i^2 = \eta_2^2 = \alpha_{\eta_2}^2 \|\text{vec}(\mathbf{H}_1)\|^2$ with respect to the original simulation setup for all $i = 1, 2, \ldots, N_I$, respectively [29]. The absolute error amounts are normalized by the norms of the vectorized signal and interferer channels for the 'D' scenario and the normalized errors are denoted by α_{η_1} and α_{η_2}. We also conduct the

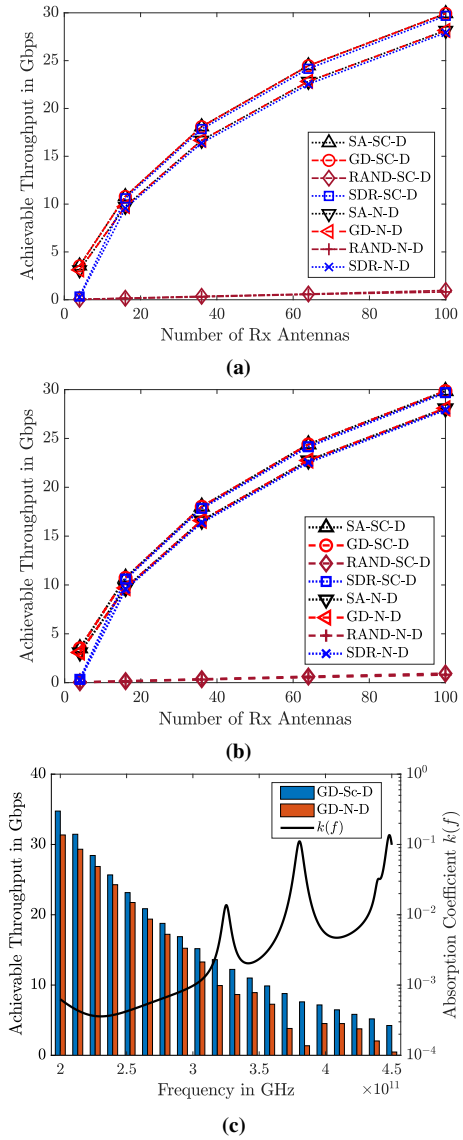

Fig. 3: Achievable throughput with the number of Rx antennas when (a) perfect ζ estimation, (b) opposite ζ estimation, and (c) frequency.

simulations under Assumption 1 and disregard BCD-SDR as it only acts as a computationally expensive baseline. In Fig. 4a, we plot SER against α_{η_1}. The SER curves of both robust and non-robust algorithms overlap implying that the robust algorithms have limited benefits when signal link has error. In Fig. 4b, we plot SER with interferer error α_{η_2}. When interferer direct links are absent, the non-robust BCD-SA algorithm results in significantly worse SER than other algorithms, while robust ones perform well. SER performance deteriorates with increasing error, and robust algorithms exhibit limited improvement when interferer links aren't blocked. BCD-GD outperforms BCD-SA as the GD solution aids RIS in suppressing interference, unlike SA, which only aligns signal channels.

Effect of interferers with imperfect CSI on SER: For a more practical scenario, SER is plotted against the number of interferers under no signal error and high interferer channel error ($\alpha_{\eta_2} = 0.0044$) in Fig. 4c. This is a practical use-

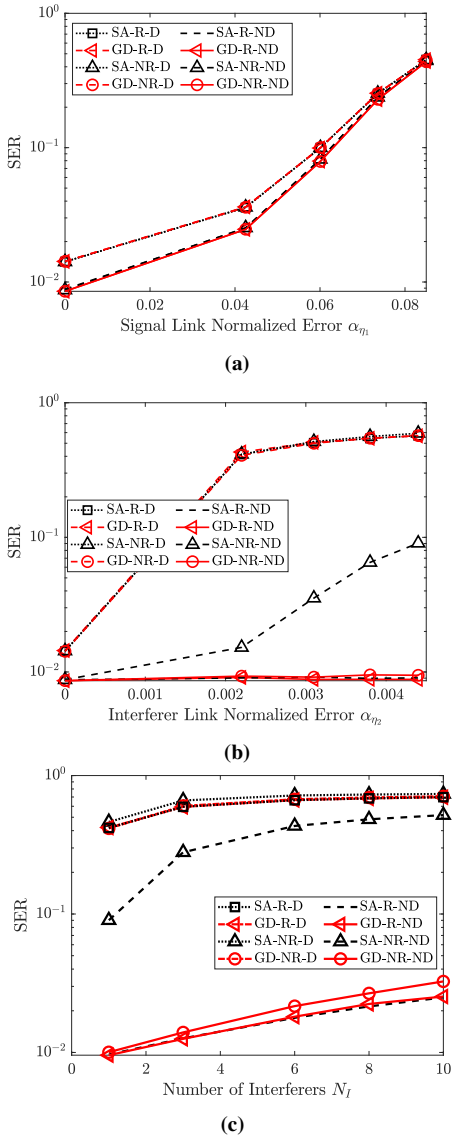

Fig. 4: Achievable throughput with the (a) normalized signal error amount, (b) normalized interferer error amount, and (c) SER with the number of interferers.

case when the interferers are non-cooperative and the Rx has limited information about the interferer channels. Further, the interferers are distributed randomly in a uniform manner on a circular ring of radius 2 meter with Rx_0 as the center. This figure shows robust algorithms outperforming non-robust counterparts in both scenarios. The performance gap decreases with more interferers when direct links are present, but increases when direct links are blocked, highlighting BCD-GD's effectiveness with non-cooperative interferers without direct links to the Rx.

Effect of transmission frequency on achievable throughput: We plot achievable throughput with the frequency in Fig. 3c. As there is not much gap between assumptions in the 'ND' scenario, we focus our discussion on the 'D' scenario. Fig. 3c illustrates that increasing carrier frequency shows a general trend of decreasing throughput performance. Although this is true for Assumption 2, it does not hold for Assumption 1 around the absorption peaks. For example, at the 380 GHz peak, throughput performance dips due to high re-radiation noise for Assumption 1, but increasing carrier frequency improves it.

V. Conclusions

In this work, we investigated the performance and sensitivity of an RIS-aided THz system under two extreme manifestations of molecular re-radiation. In particular, we first developed a unified parametric approach to study the effect of these two manifestations on the LOS THz channel model. We then jointly optimized the RIS's phase-shift and receive beamformer to maximize a lower bound on channel capacity that considers imperfect CSI. Specifically, we proposed an alternating BCD optimization framework that splits the original problem into two sub-problems: a) receive beamformer, and b) RIS optimization. These two sub-problems are then solved iteratively to converge to an efficient solution. In this framework, we approached the RIS sub-problem from three different directions: a) an SDR method that reformulates the sub-problem as a convex optimization problem while relaxing some constraints, and finds a near-optimal solution with high computational complexity, b) a fast SA method that maximizes the received power, and c) a GD-based method that converges to a first-order stationary point of the original non-convex sub-problem. Our analytical results for a one-element RIS-aided system in the presence of a single interferer demonstrated that the SA solution is sub-optimal when the direct link of the interferer has comparable power to the reflected links. Key insights from numerical results include: higher throughput and negligible impact of absorption coefficient peaks in scattering manifestation of re-radiation, dependence of throughput difference on LOS probability and frequency, minimal performance loss due to incorrect re-radiation model assumptions under perfect CSI, linear and logarithmic throughput trends against RIS elements and Rx antennas, better SER with robust algorithms when interferer links are blocked, and the efficacy of BCD-GD algorithm in non-cooperative interferer scenarios. This paper is the first to explore performance sensitivity in optimized RIS-assisted THz systems due to varying molecular re-radiation assumptions. Results indicate limited passive RIS capability against powerful interference, suggesting active RIS as a promising future research direction.

Appendix

A. Proof of Lemma 1

To begin with, the molecular absorption noise variance for the Tx_i along the direct path $\sigma^2_{m_1,i} = \mathcal{I}_i \left(\frac{c}{4\pi f d_i}\right)^2 P_i[1 - \tau(f, d_i)]$ is calculated from (7). The indicator function ensures that the noise exists only when the direct link is present. Next, we inspect the signal x of power P_i through the m-th element of a general RIS with reflection coefficient $(\alpha_m e^{j\theta_m})$ without including path-loss terms for simplicity. The incident signal on the RIS is $x\sqrt{\tau(f, d_{\gamma_i})} + n_1$, where $n_1 \sim \mathcal{CN}(0, P_i(1 - \tau(f, d_{\gamma_i})))$ is the additive molecular absorption noise. Ultimately, the reflected signal from RIS

is $y = x\sqrt{\tau(f,d_{\gamma_i})} + n_1)\alpha_m e^{j\theta_m}\sqrt{\tau(f,d_\alpha)} + n_2$. As the reflected power from the RIS element is $|\alpha_m|^2 P_i$, $n_2 \sim \mathcal{CN}(0, |\alpha_m|^2 P_i(1-\tau(f,d_\alpha)))$ is the additive noise for the RIS to Rx_0 path. So, the noise variance due to both the paths is

$$\begin{aligned}&\mathrm{E}[|n_1\alpha_m e^{j\theta_m}\sqrt{\tau(f,d_\alpha)} + n_2|^2]\\ &= |\alpha_m|^2\tau(f,d_\alpha)P_i(1-\tau(f,d_{\gamma_i})) + |\alpha_m|^2 P_i(1-\tau(f,d_\alpha))\\ &= P_i|\alpha_m|^2[1-\tau(f,d_\alpha)\tau(f,d_{\gamma_i})].\end{aligned}$$

For an N-element RIS in URA pattern with RIS-Rx_0 and Tx_i-RIS channels as $\mathbf{a}_{h_1}$, and $\mathbf{a}_{h_2}$ with their entries as $a_{h_{1,m}}$ and $a_{h_{2,m}}$, the received signal for SISO is

$$y = x\sqrt{\tau(f,d_{\gamma_i})\tau(f,d_\alpha)}\sum_{m=1}^{N}\alpha_m e^{j(\theta_m + a_{h_{1,m}} + a_{h_{2,m}})} + \sum_{m=1}^{N} n_m,$$

where

$$\sum_{m=1}^{N} n_m \sim \mathcal{CN}(0, P_i[1-\tau(f,d_\alpha)\tau(f,d_{\gamma_i})]\sum_{m=1}^{N}|\alpha_m|^2).$$

By including path-loss terms, and writing $\sum_{m=1}^{N}|\alpha_m|^2$ in matrix form, the molecular noise variance for the reflected signal through RIS can be written as $\sigma^2_{m_2,i}\boldsymbol{\theta}^H\boldsymbol{\theta}$ where $\sigma^2_{m_2,i} = \left(\frac{c^2}{16(\pi f)^2}\frac{1}{d_\alpha d_{\gamma_i}}\right)^2 P_i[1-\tau(f,d_\alpha)\tau(f,d_{\gamma_i})]$. Note that, this lemma is proved considering a general RIS which induces the inclusion of the amplitude factor α_m. However, as this work deals with the more practical choice $\alpha_m = 1$, we can substitute $\boldsymbol{\theta}^H\boldsymbol{\theta}$ with N. The molecular absorption noise variance is then $\zeta\sigma^2_{m,i}$, where $\sigma^2_{m,i} = \sigma^2_{m_1,i} + N\sigma^2_{m_2,i}$ as this noise will only exist for Assumption 1 or $\zeta = 1$.

B. Proof of Theorem 1

We start with the generic SINR expression: $\gamma_{oe} = \frac{L'+M'\cos(s+x)}{N'+P'\cos(t+x)}$ and differentiate it with respect to x and equating it to zero results in the following equations:

$$\begin{aligned}&\frac{L'+M'\cos(s+x)}{N'+P'\cos(t+x)} = \frac{M'\sin(s+x)}{P'\sin(t+x)}\\ &\implies \frac{\sin(t+x)}{M'N'} - \frac{\sin(s+x)}{L'P'} = \frac{\sin(s-t)}{L'N'}. \qquad (25)\end{aligned}$$

Using (25), the SINR can be expressed as a function of $\sin(t+x)$: $\gamma_{oe} = \frac{L'}{N'} - \frac{M'\sin(s-t)}{N'\sin(t+x)}$. The solutions for $\sin(t+x)$ plugged in this SINR expression proves the theorem. Note that the solution for $\sin(t+x)$ is found by expressing (25) as a quadratic equation by the simple observation that $t+x = (s+x)-(s-t)$.

REFERENCES

[1] A. Pradhan, J. K. Devineni, H. S. Dhillon, and A. F. Molisch, "Intelligent Surface Optimization in Terahertz under Two Manifestations of Molecular Re-radiation," in *Proc., IEEE Globecom*, Dec. 2021.

[2] S. Tripathi, N. V. Sabu, A. K. Gupta, and H. S. Dhillon, "Millimeter-wave and Terahertz Spectrum for 6G Wireless," in *6G Mobile Wireless Networks*, Y. Wu, S. Singh, T. Taleb, A. Roy, H. S. Dhillon, M. R. Kanagarathinam, and A. De, Eds. Springer, 2021.

[3] J. G. Andrews, S. Buzzi, W. Choi, S. V. Hanly, A. Lozano, A. C. K. Soong, and J. C. Zhang, "What Will 5G Be?" *IEEE Journal on Sel. Areas in Commun.*, vol. 32, no. 6, pp. 1065–1082, June 2014.

[4] H. Tataria, M. Shafi, A. F. Molisch, M. Dohler, H. Sjöland, and F. Tufvesson, "6G Wireless Systems: Vision, Requirements, Challenges, Insights, and Opportunities," *Proc. of the IEEE*, vol. 109, no. 7, pp. 1166–1199, July 2021.

[5] F. Anwar, C. Carlos, V. Saraswat, V. Mangu, M. Arnold, and F. Cavallo, "Nanoscale Graphene/Ge Wigglers as Building Blocks for THz Sources," *Aip Advances*, vol. 7, no. 11, Nov. 2017.

[6] K. Ahi, "Review of GaN-based Devices for Terahertz Operation," *Optical Engineering*, vol. 56, no. 9, pp. 1–14, Sep. 2017.

[7] C. Chaccour, M. N. Soorki, W. Saad, M. Bennis, and P. Popovski, "Risk-Based Optimization of Virtual Reality over Terahertz Reconfigurable Intelligent Surfaces," in *Proc., IEEE Intl. Conf. on Commun. (ICC)*, June 2020.

[8] J. Kokkoniemi, J. Lehtomäki, and M. Juntti, "A Discussion on Molecular Absorption Noise in the Terahertz Band," *Nano commun. networks*, vol. 8, pp. 35–45, June 2016.

[9] Y. Yang, M. Mandehgar, and D. Grischkowsky, "Determination of the water vapor continuum absorption by THz-TDS and Molecular Response Theory," *Opt. Express*, vol. 22, no. 4, pp. 4388–4403, Feb. 2014.

[10] A. F. Molisch and B. P. Oehry, *Radiation Trapping in Atomic Vapours*. Oxford University Press, 1998.

[11] J. M. Jornet and I. F. Akyildiz, *Fundamentals of Electromagnetic Nanonetworks in the Terahertz Band*. Now Foundations and Trends, 2013.

[12] H. Harde and D. Grischkowsky, "Coherent Transients Excited by Subpicosecond Pulses of Terahertz Radiation," *J. Opt. Soc. Am. B*, vol. 8, no. 8, pp. 1642–1651, Aug. 1991.

[13] H. Harde, R. Cheville, and D. Grischkowsky, "Terahertz Studies of Collision-Broadened Rotational Lines," *J. Phys. Chem. A*, vol. 101, no. 20, pp. 3646–3660, May 1997.

[14] S. A. Hoseini, M. Ding, M. Hassan, and Y. Chen, "Analyzing the Impact of Molecular Re-Radiation on the MIMO Capacity in High-Frequency Bands," *IEEE Trans. on Veh. Technology*, vol. 69, no. 12, pp. 15 458–15 471, Dec. 2020.

[15] Q. Wu and R. Zhang, "Beamforming Optimization for Wireless Network Aided by Intelligent Reflecting Surface with Discrete Phase Shifts," *IEEE Trans. on Commun.*, vol. 68, no. 3, pp. 1838–1851, Dec. 2019.

[16] J. Yuan, Y.-C. Liang, J. Joung, G. Feng, and E. G. Larsson, "Intelligent Reflecting Surface-Assisted Cognitive Radio System," *IEEE Trans. on Commun.*, vol. 69, no. 1, pp. 675–687, Oct. 2020.

[17] J. Ye, S. Guo, and M.-S. Alouini, "Joint Reflecting and Precoding Designs for SER Minimization in Reconfigurable Intelligent Surfaces Assisted MIMO Systems," *IEEE Trans. on Wireless Commun.*, vol. 19, no. 8, pp. 5561–5574, May 2020.

[18] R. Long, Y.-C. Liang, Y. Pei, and E. G. Larsson, "Active Reconfigurable Intelligent Surface-Aided Wireless Communications," *IEEE Trans. on Wireless Commun.*, vol. 20, no. 8, pp. 4962–4975, Mar. 2021.

[19] X. Yu, D. Xu, and R. Schober, "Enabling Secure Wireless Communications via Intelligent Reflecting Surfaces," in *Proc., IEEE Globecom*, Dec. 2019.

[20] C. Huang, A. Zappone, G. C. Alexandropoulos, M. Debbah, and C. Yuen, "Reconfigurable Intelligent Surfaces for Energy Efficiency in Wireless Communication," *IEEE Trans. on Wireless Commun.*, vol. 18, no. 8, pp. 4157–4170, June 2019.

[21] A. Pradhan and H. S. Dhillon, "A Probabilistic Reformulation Technique for Discrete RIS Optimization in Wireless Systems," *arXiv:2303.00182*, 2023.

[22] X. Ma, Z. Chen, W. Chen, Y. Chi, Z. Li, C. Han, and Q. Wen, "Intelligent Reflecting Surface Enhanced Indoor Terahertz Communication Systems," *Nano Commun. Networks*, vol. 24, p. 100284, Feb. 2020.

[23] Y. Pan, K. Wang, C. Pan, H. Zhu, and J. Wang, "Sum Rate Maximization for Intelligent Reflecting Surface Assisted Terahertz Communications," *arXiv:2008.12246*, 2020.

[24] K. Dovelos, S. D. Assimonis, H. Quoc Ngo, B. Bellalta, and M. Matthaiou, "Intelligent Reflecting Surfaces at Terahertz Bands: Channel Modeling and Analysis," in *Proc., IEEE Intl. Conf. on Commun. Workshops (ICC Workshops)*, June 2021.

[25] B. Ning, Z. Chen, W. Chen, and L. Li, "Improving Security of THz Communication with Intelligent Reflecting Surface," in *Proc., IEEE Globecom Workshops*, Dec. 2019.

[26] H. Du, J. Zhang, K. Guan, D. Niyato, H. Jiao, Z. Wang, and T. Kürner, "Performance and Optimization of Reconfigurable Intelligent Surface Aided THz Communications," *IEEE Trans. on Commun.*, vol. 70, no. 5, pp. 3575–3593, Mar. 2022.

[27] K. Tekbıyık, G. K. Kurt, A. R. Ekti, and H. Yanikomeroglu, "Reconfigurable Intelligent Surfaces Empowered THz Communication in LEO Satellite Networks," *arXiv:2007.04281*, 2020.

[28] W. Hao, G. Sun, M. Zeng, Z. Chu, Z. Zhu, O. A. Dobre, and P. Xiao, "Robust Design for Intelligent Reflecting Surface-Assisted MIMO-OFDMA Terahertz IoT Networks," *IEEE Internet of Things Journal*, vol. 8, no. 16, pp. 13 052–13 064, Mar. 2021.

[29] Z. Zhu, J. Xu, G. Sun, W. Hao, Z. Chu, C. Pan, and I. Lee, "Robust Beamforming Design for IRS-Aided Secure SWIPT Terahertz Systems With Non-Linear EH Model," *IEEE Wireless Commun. Letters*, vol. 11, no. 4, pp. 746–750, Jan 2022.

[30] J. Qiao, C. Zhang, A. Dong, J. Bian, and M.-S. Alouini, "Securing Intelligent Reflecting Surface Assisted Terahertz Systems," *IEEE Trans. on Veh. Technology*, May 2022.

[31] Y. Ma, Y. Shen, X. Yu, J. Zhang, S. Song, and K. B. Letaief, "A Low-Complexity Algorithmic Framework for Large-Scale IRS-Assisted Wireless Systems," in *Proc., IEEE Globecom Workshops*, Dec. 2020.

[32] E. Björnson, J. Hoydis, and L. Sanguinetti, *Massive MIMO Networks: Spectral, Energy, and Hardware Efficiency*. Now Foundations and Trends, 2017.

[33] C. Guo, L. Zhao, Y. Cui, Z. Liu, and D. W. K. Ng, "Power-Efficient Wireless Streaming of Multi-Quality Tiled 360 VR Video in MIMO-OFDMA Systems," *IEEE Trans. on Wireless Commun.*, vol. 20, no. 8, pp. 5408–5422, Mar. 2021.

[34] C. Chaccour, R. Amer, B. Zhou, and W. Saad, "On the Reliability of Wireless Virtual Reality at Terahertz (THz) Frequencies," in *2019 10th IFIP International Conference on New Technologies, Mobility and Security (NTMS)*, June 2019.

[35] Z. Hossain, C. N. Mollica, J. F. Federici, and J. M. Jornet, "Stochastic Interference Modeling and Experimental Validation for Pulse-Based Terahertz Communication," *IEEE Trans. on Wireless Commun.*, vol. 18, no. 8, pp. 4103–4115, Aug. 2019.

[36] R. J. Williams, E. de Carvalho, and T. L. Marzetta, "A Communication Model for Large Intelligent Surfaces," in *Proc., IEEE Intl. Conf. on Commun. Workshops (ICC Workshops)*, June 2020.

[37] J. Kokkoniemi, J. Lehtomäki, and M. Juntti, "Simple Molecular Absorption Loss Model for 200–450 Gigahertz Frequency Band," in *European Conf. on Networks and Commun. (EuCNC)*, June 2019.

[38] H. Do, S. Cho, J. Park, H.-J. Song, N. Lee, and A. Lozano, "Terahertz Line-of-Sight MIMO Communication: Theory and Practical Challenges," *IEEE Commun. Magazine*, vol. 59, no. 3, pp. 104–109, Mar. 2021.

[39] O. A. Alduchov and R. E. Eskridge, "Improved Magnus Form Approximation of Saturation Vapor Pressure," *Journal of Applied Meteorology and Climatology*, vol. 35, no. 4, pp. 601 – 609, Apr. 1996.

[40] M. van Exter, C. Fattinger, and D. Grischkowsky, "Terahertz Time-domain Spectroscopy of Water Vapor," *Opt. Lett.*, vol. 14, no. 20, pp. 1128–1130, Oct. 1989.

[41] S. Priebe, M. Kannicht, M. Jacob, and T. Kürner, "Ultra broadband indoor channel measurements and calibrated ray tracing propagation modeling at THz frequencies," *Journal of Commun. and Networks*, vol. 15, no. 6, pp. 547–558, Dec. 2013.

[42] C. Pan, G. Zhou, K. Zhi, S. Hong, T. Wu, Y. Pan, H. Ren, M. D. Renzo, A. Lee Swindlehurst, R. Zhang, and A. Y. Zhang, "An Overview of Signal Processing Techniques for RIS/IRS-Aided Wireless Systems," *IEEE Journal of Sel. Topics in Signal Processing*, vol. 16, no. 5, pp. 883–917, Aug. 2022.

[43] Y. Li, A. C. K. Soong, Y. Du, and J. Lu, "Beamforming with Imperfect CSI," in *Proc., IEEE Wireless Commun. and Networking Conf. (WCNC)*, Mar. 2007.

[44] N. Nandan, S. Majhi, and H.-C. Wu, "Beamforming and Power Optimization for Physical Layer Security of MIMO-NOMA Based CRN Over Imperfect CSI," *IEEE Trans. on Veh. Technology*, vol. 70, no. 6, pp. 5990–6001, June 2021.

[45] A. Gründinger, *Models for Incomplete Channel Knowledge*. Cham: Springer International Publishing, Dec. 2020, pp. 29–38.

[46] S. Abu-Surra, W. Choi, S. Choi, E. Seok, D. Kim, N. Sharma, S. Advani, V. Loseu, K. Bae, I. Na, A. A. Farid, M. J. W. Rodwell, G. Xu, and J. C. Zhang, "End-to-end 140 GHz Wireless Link Demonstration with Fully-Digital Beamformed System," in *Proc., IEEE Intl. Conf. on Commun. Workshops (ICC Workshops)*, June 2021.

[47] D. Tse and P. Viswanath, *Fundamentals of Wireless Communication*. Cambridge University Press, 2005.

[48] D. P. Palomar and Y. C. Eldar, *Convex Optimization in Signal Processing and Communications*. Cambridge university press, 2010.

[49] M. Grant and S. Boyd. (2014, Mar.) CVX: Matlab Software for Disciplined Convex Programming, version 2.1. [Online]. Available: http://cvxr.com/cvx

[50] ——, "Graph implementations for nonsmooth convex programs," in *Recent Advances in Learning and Control*, ser. Lecture Notes in Control and Information Sciences, V. Blondel, S. Boyd, and H. Kimura, Eds. Springer-Verlag Limited, 2008, pp. 95–110.

[51] Z.-q. Luo, W.-k. Ma, A. M.-c. So, Y. Ye, and S. Zhang, "Semidefinite Relaxation of Quadratic Optimization Problems," *IEEE Signal Processing Magazine*, vol. 27, no. 3, pp. 20–34, Apr. 2010.

[52] B. Feng, J. Gao, Y. Wu, W. Zhang, X.-G. Xia, and C. Xiao, "Optimization Techniques in Reconfigurable Intelligent Surface Aided Networks," *IEEE Wireless Commun.*, vol. 28, no. 6, pp. 87–93, Dec. 2021.

[53] I. Panageas, G. Piliouras, and X. Wang, "First-order methods almost always avoid saddle points: The case of vanishing step-sizes," *Advances in Neural Info. Processing Systems*, vol. 32, 2019.

[54] S. S. Du, C. Jin, J. D. Lee, M. I. Jordan, A. Singh, and B. Poczos, "Gradient Descent Can Take Exponential Time to Escape Saddle Points," *Advances in Neural Info. Processing Systems*, vol. 30, 2017.

[55] J. Nocedal and S. J. Wright, *Numerical optimization*. Springer, 1999.

[56] Y. Zhang, G. Zhang, and X. Wang, "Computationally Efficient DOA Estimation for Monostatic MIMO Radar Based on Covariance Matrix Reconstruction," *Electronics Letters*, vol. 53, no. 2, pp. 111–113, Jan. 2017.

[57] B. Kalantari, "On the Equivalence of SDP Feasibility and a Convex Hull Relaxation for System of Quadratic Equations," *arXiv:1911.03989*, 2019.

[58] K. Sikorski, "Bisection is Optimal," *Numerische Mathematik*, vol. 40, no. 1, pp. 111–117, Feb. 1982.

[59] P. Rodríguez-Vázquez, J. Grzyb, B. Heinemann, and U. R. Pfeiffer, "A 16-QAM 100-Gb/s 1-M Wireless Link With an EVM of 17% at 230 GHz in an SiGe Technology," *IEEE Microwave and Wireless Components Letters*, vol. 29, no. 4, pp. 297–299, Mar. 2019.

Anish Pradhan (Graduate Student Member, IEEE) received the B.Tech degree in Electronics and Communication Engineering from the National Institute of Technology Durgapur, India, in 2018. He is currently pursuing a Ph.D. degree at the Bradley Department of Electrical and Computer Engineering, Virginia Tech, USA. His current research interests include MIMO, optimization theory, and reconfigurable intelligent surfaces.

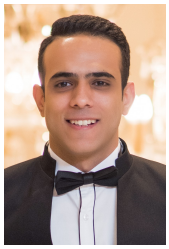

Mohamed A. Abd-Elmagid (Member, IEEE) received the B.Sc. degree in electronics and electrical communications engineering from Cairo University in 2014, the M.S. degree in wireless communications from Nile University in 2017, and the Ph.D. degree in electrical engineering from Virginia Tech in 2023. He is currently a postdoctoral researcher in the electrical and computer engineering department at the Ohio State University. His research interests include age of information, energy harvesting, queueing theory, optimization, machine learning, and stochastic geometry. He is the recipient of the WiOpt 2021 best student paper award.

Harpreet S. Dhillon (Fellow, IEEE) received the B.Tech. degree in electronics and communication engineering from IIT Guwahati in 2008, the M.S. degree in electrical engineering from Virginia Tech in 2010, and the Ph.D. degree in electrical engineering from the University of Texas at Austin in 2013.

After serving as a Viterbi Postdoctoral Fellow at the University of Southern California for a year, he joined Virginia Tech in 2014, where he is currently a Professor of electrical and computer engineering, the chair of the communications area, the Associate Director of Wireless@VT research group, and the Elizabeth and James E. Turner Jr. '56 Faculty Fellow. His research interests include communication theory, wireless networks, geolocation, and stochastic geometry. He is a fellow of AAIA and a Clarivate Analytics (Web of Science) Highly Cited Researcher. He has received six best paper awards including the 2014 IEEE Leonard G. Abraham Prize, the 2015 IEEE ComSoc Young Author Best Paper Award, and the 2016 IEEE Heinrich Hertz Award. He has also received Early Achievement Awards from three IEEE ComSoc Technical Committees, namely, the Communication Theory Technical Committee (CTTC) in 2020, the Radio Communications Committee (RCC) in 2020, and the Wireless Communications Technical Committee (WTC) in 2021. He was named the 2017 Outstanding New Assistant Professor, the 2018 Steven O. Lane Junior Faculty Fellow, the 2018 College of Engineering Faculty Fellow, and the recipient of the 2020 Dean's Award for Excellence in Research by Virginia Tech. His other academic honors include the 2008 Agilent Engineering and Technology Award, the UT Austin MCD Fellowship, the 2013 UT Austin WNCG leadership award, and the inaugural IIT Guwahati Young Alumni Achiever Award 2020. He has served as the TPC Co-chair for IEEE WCNC 2022 and as a symposium TPC Co-chair for many IEEE conferences. He has also served on the Editorial boards of several IEEE journals with his current appointments being on the Executive Editorial Committee for IEEE TRANSACTIONS ON WIRELESS COMMUNICATIONS and as a Senior Editor for IEEE WIRELESS COMMUNICATIONS LETTERS.

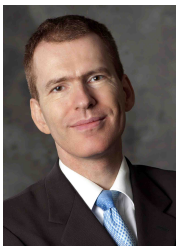

Andreas F. Molisch (Fellow, IEEE) received his degrees (Dipl.Ing. 1990, PhD 1994, Habilitation 1999) from the Technical University Vienna, Austria. He spent the next 10 years in industry, at FTW, AT&T (Bell) Laboratories, and Mitsubishi Electric Research Labs (where he rose to Chief Wireless Standards Architect). In 2009 he joined the University of Southern California (USC) in Los Angeles, CA, as Professor, and founded the Wireless Devices and Systems (WiDeS) group. In 2017, he was appointed to the Solomon Golomb – Andrew and Erna Viterbi Chair.

His research interests revolve around wireless propagation channels, wireless systems design, and their interaction. Recently, his main interests have been wireless channel measurement and modeling for 5G and beyond 5G systems, joint communication-caching-computation, hybrid beamforming, UWB/TOA based localization, and novel modulation/multiple access methods. Overall, he has published 5 books (among them the textbook "Wireless Communications", third edition in 2022), 22 book chapters, 300 journal papers, and 400 conference papers. He is also the inventor of 70 granted (and more than 10 pending) patents, and co-author of some 70 standards contributions. His work has been cited more than 64,000 times, his h-index is 106, and he is a Clarivate Highly Cited Researcher.

Dr. Molisch has been an Editor of a number of journals and special issues, General Chair, Technical Program Committee Chair, or Symposium Chair of multiple international conferences, as well as Chairperson of various international standardization groups. He is a Fellow of the National Academy of Inventors, Fellow of the AAAS, Fellow of the IEEE, Fellow of the IET, an IEEE Distinguished Lecturer, and a member of the Austrian Academy of Sciences. He has received numerous awards, among them the IET Achievement Medal, the Technical Achievement Awards of IEEE Vehicular Technology Society (Evans Avant-Garde Award) and the IEEE Communications Society (Edwin Howard Armstrong Award), and the Technical Field Award of the IEEE for Communications, the Eric Sumner Award.